Thermally Induced Convective Circulation and Precipitation over an Isolated Volcano

ALEXANDROS P. POULIDIS AND IAN A. RENFREW

Centre for Ocean and Atmospheric Sciences, School of Environmental Sciences, University of East Anglia, Norwich, United Kingdom

ADRIAN J. MATTHEWS

Centre for Ocean and Atmospheric Sciences, School of Environmental Sciences, and School of Mathematics, University of East Anglia, Norwich, United Kingdom

(Manuscript received 31 October 2014, in final form 12 June 2015)

ABSTRACT

Intense rainfall over active volcanoes is known to trigger dangerous volcanic hazards, from remobilizing loose volcanic surface material into lahars or mudflows to initiating explosive activity including pyroclastic flows at certain dome-forming volcanoes. However, the effect of the heated volcanic surface on the atmospheric circulation, including any feedback with precipitation, is unknown. This is investigated here, using the Weather Research and Forecasting (WRF) Model. The recent activity at the Soufrière Hills Volcano (SHV), Montserrat, is a well-documented case of such rainfall–volcano interaction and is used as a template for these experiments. The volcano is represented in the model by an idealized Gaussian mountain, with an imposed realistic surface temperature anomaly on the volcano summit. A robust increase in precipitation over the volcano is simulated for surface temperature anomalies above approximately 40°C, an area-average value that is exceeded at the SHV. For wind speeds less than 4 m s^{-1} and a range of realistic atmospheric conditions, the precipitation increase is well above the threshold required to trigger volcanic hazards (5–10 mm h^{-1}). Hence, the thermal atmospheric forcing due to an active, but nonerupting, volcano appears to be an important factor in rainfall–volcano interactions and should be taken account of in future hazard studies.

1. Introduction

Rainfall is a well-established trigger for volcanic hazards. This link is self-evident for ''secondary'' volcanic activity such as lahars—volcanic mudflows composed of remobilized volcanic sediment and rainwater (Major and Newhall 1989; Smith and Fritz 1989). Perhaps unexpectedly, rainfall can also trigger ''primary'' volcanic activity such as pyroclastic flows and volcanic dome collapses, as documented at Mount St. Helens, United States (Mastin 1994); Unzen, Japan (Yamasato et al. 1998); Merapi, Indonesia (Voight et al. 2000); Piton de la Fournaise, Réunion Island (Violette et al. 2001); Soufrière Hills Volcano (SHV), Montserrat (Matthews et al. 2002; Carn et al. 2004; Barclay et al. 2006; Matthews et al. 2009); and Stromboli, Italy (Hort et al. 2003). There is, however, a further unexplored possibility: that the heated summit of a volcano interacts with the orographic flow to force atmospheric convection and enhance precipitation, thus potentially creating a positive feedback. Here we will examine this possibility through numerical modeling.

Orographic flow in the vicinity of hills and ridges is a classic problem in meteorology (e.g., Queney 1948; Eliassen and Palm 1961; Drazin 1961; Smith 1980, 1989; Smolarkiewicz and Rotunno 1989; Ólafsson and Bougeault 1996). However, orographic flow over heated topography has not been as widely studied. The main rationale behind previous research has been to investigate the impact of solar heating in triggering localized convective updrafts and their effect on weather systems (Crook and Tucker 2005; Lewis et al. 2008; Kirshbaum 2011). The general result is a generation or strengthening of severe storms akin to the way mountains can enhance rainfall (Crook and Tucker 2005; Kirshbaum 2011). Although linear theory has been used to study the effect of sufficiently weak thermal forcing (Crook

Corresponding author address: Alexandros P. Poulidis, School of Environmental Sciences, University of East Anglia, Room ENV 3.16, Norwich Research Park, Norwich NR4 7TJ, United Kingdom. E-mail: a.poulidis@uea.ac.uk

DOI: 10.1175/JAS-D-14-0327.1

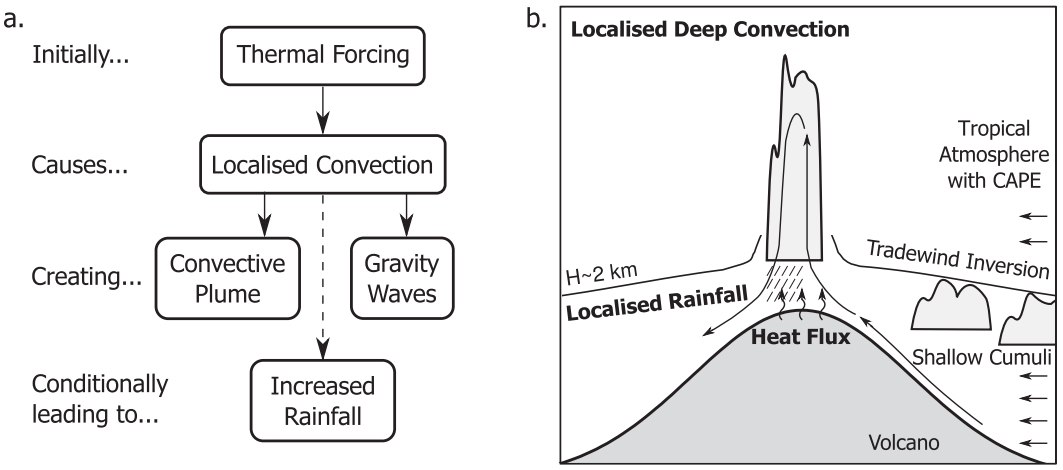

FIG. 1. (a) Conceptual model under study. (b) Schematic describing the proposed mechanism: a background of easterlies with a shallow cumulus field under the trade wind inversion meets the volcano. The flow over the summit of the volcano is heated and locally breaks through the inversion, resulting in deep convection and high local rainfall rates.

and Tucker 2005; Tucker and Crook 2005), Kirshbaum (2013) demonstrated that the application of linear theory for two layer flows is severely limited owing to the nonlinear effects that are introduced by the difference between the layers.

Recently, attention has focused on the impact of wild fires in the generation of pyrocumulus clouds (Gatebe et al. 2012) and the initialization of storms (Cunningham and Reeder 2009). Wild fires lead to a localized maximum in surface temperature, along with the release of water vapor and chemical byproducts from burning. Depending on the atmospheric structure, they can generate deep convection, pyrocumulus clouds, and severe storms. As in the solar heating cases, the result is a localized convection cell that can break through the convective inhibition of the lower atmosphere and force deep convection. Unlike the solar heating cases, these storms often occur under strong winds, but the extension and propagation of the storm still depends heavily on the atmospheric structure (Cunningham and Reeder 2009).

We have a different rationale for studying the effects of heated terrain on the atmosphere: examining how a volcano can influence the atmospheric flow. The focus of this study is on flows over active dome-building volcanoes, not undergoing an explosive eruption. Dome-building volcanoes extrude high-viscosity magma through a central conduit, which cools and solidifies, blocking further flow up the conduit and forming a pressurized lava dome. This lava dome can become unstable owing to a combination of its own gravitational weight and internal pressure from within the volcanic system. Subsequent failure of the lava dome can lead to explosive dome collapse and pyroclastic flows. Heavy rainfall has been implicated in triggering some such dome collapses and pyroclastic flows at a number of volcanoes, including SHV, Montserrat (Matthews et al. 2002). Several mechanisms have been hypothesized for this rainfall triggering, including mechanical erosion of the surrounding talus fan and gravitational destabilization of the dome, or the formation of a rainfall-saturated cap that blocks the upward flow of magmatic gas, leading to a pressurized failure (Matthews and Barclay 2004; Hicks et al. 2010, 2014). Hence, any enhancement of rainfall by the heated surface of the volcanic dome may lead to a positive feedback, increasing the probability of these dangerous volcanic hazards.

In this study, an atmospheric model is used to simulate the effect of the heated volcanic surface on the atmospheric circulation and associated rainfall. The numerical experiments presented here are generalized but are carried out for the tropical atmospheric conditions representative of those at SHV, Montserrat, where such rainfall–volcanic interactions are well established. It is worth noting that nearly half of the approximately 1500 active or potentially active volcanoes in the world lie in the tropics (Simkin and Siebert 1994).

The conceptual model being tested assumes a trade wind cumulus regime in an easterly background flow with a trade wind inversion (Fig. 1). Note that the trade wind inversion here is defined by the height of the thermal inversion in the atmosphere. The flow over the top of the volcano is subject to thermal forcing via the surface fluxes from the strongly heated volcanic surface. This is hypothesized to be sufficient for convective plumes to break through the inversion, releasing the high values of convective available potential energy

(CAPE) present in the background state and initiating intense localized rainfall over the volcano. Although beyond the scope of this study, this enhanced rainfall may then trigger an already unstable volcanic dome to collapse (by the mechanisms described above) or trigger secondary volcanic hazards such as lahars. Volcanic emissions such as gas and ash are not accounted for and this is discussed further in section 6.

The paper is organized as follows. In section 2 a short description of the experimental setup will be presented. Section 3 presents control simulations—that is, with no surface heating. Section 4 presents the primary orographic flow response to the volcanic heating, while section 5 focuses on the structure and characteristics of the volcanically triggered storm. A discussion and conclusions are in sections 6 and 7, respectively.

2. Experimental configuration

a. Location

The Soufrière Hills Volcano, Montserrat, has been chosen as the "template" for the idealized simulations presented here. Montserrat is located in the tropics at 16.75°N, 62.20°W, and is part of the Lesser Antilles, in the eastern Caribbean. It has been volcanically active since 1995, with a series of devastating eruptions and active dome-building cycles over the last 20 years. For an overview of related research, see Sparks and Young (2002) and Wadge et al. (2014).

Even though orographic rainfall, the result of air mechanically forced to ascend over a hill or mountain, can greatly affect precipitation in the tropics, it is a field that has received relatively little attention. Recent studies as part of the Dominica Experiment (DOMEX; Smith et al. 2012) have shown that, aside from diurnally forced deep convection and tropical cyclones (Houze 2012), shallow convection from mechanically forced ascent can have a significant effect on the local precipitation (Kirshbaum and Smith 2009; Minder et al. 2013). This has also been established for other islands in the Caribbean (Cécé et al. 2014). The general response can be summarized as greater cloud cover over the windward side, with enhanced convection and precipitation as the cumulus field created over the ocean interacts first with the coastline and then with the mountain. Although the specific response depends on the size and shape of each island and mountain, the resulting orographically enhanced rainfall over the windward side of the island can be substantially higher (a factor of 10) than rainfall over the sea (Kirshbaum and Smith 2009; Smith et al. 2009).

b. Model setup

The numerical simulations were carried out using the Weather Research and Forecasting (WRF) Model, version 3.3.1, running in an idealized configuration. WRF features a fully compressible, three-dimensional nonhydrostatic model, with the governing equations solved in flux form. The model adopts an Arakawa C grid, a time-splitting explicit advection scheme, and a terrain-following height coordinate (Skamarock et al. 2008). More information about the model can be found at http://www.wrf-model.org.

The model domain consists of an isolated volcano, located near the center of the domain and surrounded by ocean (Fig. 2). Note that the terms "volcano" and "mountain" are used interchangeably throughout the rest of the paper. The height h of the volcano has a Gaussian profile with a width of approximately 20 km and a height of 1 km:

$$h(x,y) = h_{\text{top}} \exp\left[-\left(\frac{x-x_s}{L_x}\right)^2 - \left(\frac{y-y_s}{L_y}\right)^2\right], \quad (1)$$

where x_s and y_s are the coordinates of the volcano's center, $h_{\text{top}} = 1000$ m is the maximum height, and L_x and L_y are characteristic horizontal length scales (both were set at 5700 m; see Fig. 2a). For $h < 1$ m, the height is explicitly set to 0 m. Although the simulations are idealized, these dimensions were chosen so that the mountain is broadly representative of volcanic islands in the Caribbean (e.g., Montserrat, St. Vincent, Dominica, Martinique, Guadeloupe). Grid points where $h > 0$ m are assigned "land" status ("barren or sparsely vegetated" category, available moisture: 2%, roughness length: 1 cm), while grid points where $h = 0$ m are assigned "water" status ("water body" category, available moisture: 100%, roughness length: 0.01 cm; see Fig. 2b). Note that there is no thermal contrast between the land and the sea, so there are no sea breeze circulations in the study.

The domain has 680 by 250 grid points with a grid spacing of $\Delta x = \Delta y = 300$ m in both directions, so representing 204 km in the x direction and 75 km in the y direction. There are 147 levels in the vertical. The vertical grid spacing is 50 m up to a height of 4 km, it increases linearly to 200 m up to a height of 12 km, and then increases linearly up to 1000 m up to the model top at 16 km. Periodic boundary conditions are chosen for all lateral boundaries. The time step is 2 s with each simulation run for 6 h. The first 3 h are spent on model "spinup" (hours 1–2) and approaching a quasi-steady state (hours 2–3). All results presented are 3-h averages from hours 3 to 6. Sensitivity tests with a smaller time

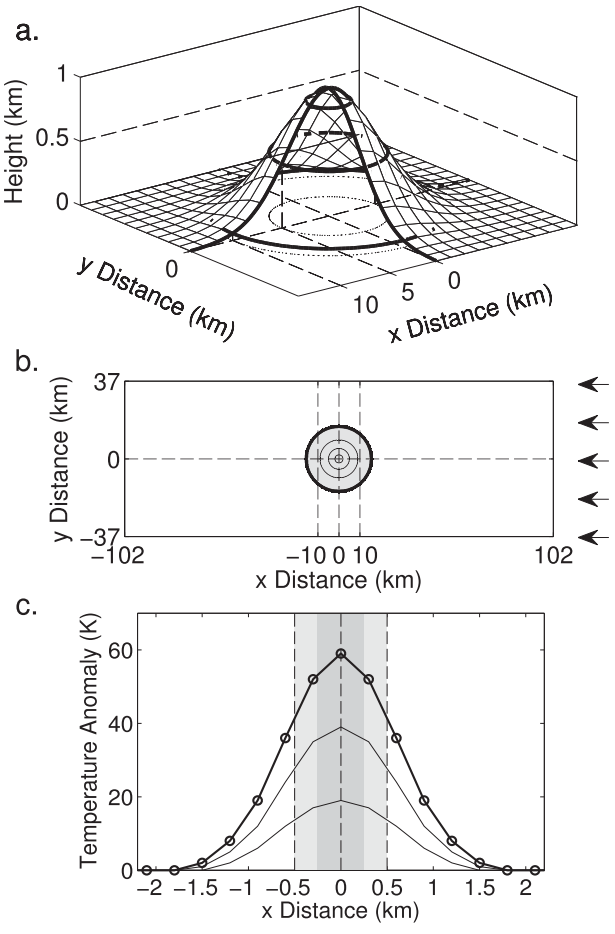

FIG. 2. (a) Cutaway of the topography of the idealized Gaussian mountain. (b) Model domain. The mountain is centered at $x = 0$, $y = 0$. Selected height contours are shown at 1 m (thick) and then at 100, 500, and 900 m (thin), corresponding to the thick contours in (a). The model surface type is land where the height is over 1 m (shaded area) and water everywhere else. The background wind is easterly, as indicated by the arrows on the right (upwind) boundary. (c) Cross section through the center of the volcano showing surface temperature anomaly (surface temperature minus ambient surface temperature). The shaded areas show typical lava-dome dimensions.

step and a longer duration (up to 9 h) showed only minor changes in the output.

A suite of physical parameterizations are implemented in WRF. The thermal diffusion land surface scheme is used to implement the surface heating on the top of the volcano (Skamarock et al. 2008). Heat and moisture fluxes are parameterized by the MM5 similarity scheme, based on Monin–Obukhov theory (Monin and Obukhov 1954) with Carlson–Boland viscous sublayer and standard similarity functions from lookup tables (Dyer and Hicks 1970; Paulson 1970; Webb 1970; Beljaars 1995). The relatively complex six-phase "Purdue–Lin" microphysics scheme is used, based on the studies by Lin et al. (1983) and Rutledge and Hobbs (1983). This scheme was chosen because deep convection past the freezing point was expected (Hong and Lin 2006).

The radiation, boundary layer, and cumulus schemes are switched off for all simulations. While it is acknowledged that diurnal effects play an important role in mesoscale circulations in the tropics, we wanted to isolate the impact of volcanic heating on the atmosphere without the complication of a diurnal cycle. The lack of a radiation scheme does not grossly affect the magnitude of the surface heat fluxes (controlled by the soil and surface layer models). As no simulations last more than 9 h and as the focus of the study is on a quasi-steady response, then not implementing a radiation scheme is appropriate. At the current resolution, the boundary layer scheme is not needed as primary eddies are explicitly resolved (Bryan et al. 2003; Kirshbaum and Fairman 2014).

Aside from these schemes, an option for diffusion that evaluates mixing terms in physical space and 1.5-order TKE closure is used in all simulations. Note that, on initiation, a random perturbation is imposed on the mean temperature field at the lower four grid levels (± 0.05 K) to kick off turbulent motion and then the atmosphere is rebalanced hydrostatically. Coriolis force is used with $f = 4 \times 10^{-5}\,\mathrm{s}^{-1}$. A Runge–Kutta third-order time scheme is used for the computations. A fifth-order and a third-order scheme are used for momentum and scalar advection, respectively, in the horizontal and vertical dimensions (Skamarock et al. 2008). A w–Rayleigh damping layer with an inverse time scale is used above 8 km to reduce the errors from spurious gravity waves being reflected on the top of the domain (Klemp et al. 2008), and sixth-order monotonic horizontal diffusion is applied to all variables for stability and to minimize spurious behavior at poorly resolved scales (Knievel et al. 2007).

c. *Initialization sounding*

All simulations have been initialized horizontally homogeneously from a prescribed atmospheric profile. Figure 3 shows the different profiles used in the study. These are based on those of Siebesma et al. (2003), which are marine soundings from the Caribbean during the BOMEX experiment, that have been simplified and used in several modeling studies (e.g., Siebesma et al. 2003; Kirshbaum and Smith 2009). Several idealized profiles have been prescribed with changes in inversion strength, tropospheric humidity, and ambient wind speed. The soundings include a temperature inversion signifying the top of the "trade wind cumulus" regime. The potential temperature profile features a neutrally

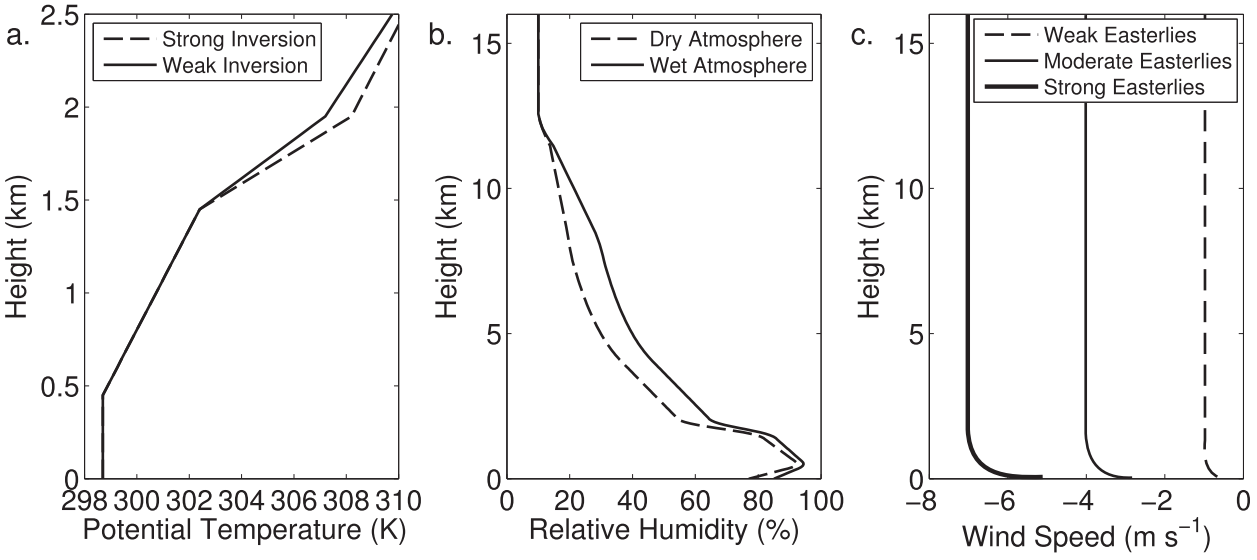

FIG. 3. Thermodynamic profiles used in the simulations. (a) Dry potential temperature profiles for weak inversion (solid line) and strong inversion (dashed line). (b) Relative humidity profiles for dry atmosphere (solid line) and wet atmosphere (dashed line). (c) Wind speed profiles for "weak easterlies" (dashed line), "moderate easterlies" (thin solid line), and "strong easterlies" (thick solid line). Note the change in vertical axis. The combination of dry atmosphere and strong inversion (referred to as dry–strong inversion here) is the profile used by Siebesma et al. (2003) and Kirshbaum and Smith (2009).

stratified layer for the first 500 m, a conditionally unstable layer between 500 and 1500 m, and a temperature inversion layer up to 2000 m. The difference in the maximum potential temperature θ_I between the "strong inversion" and "weak inversion" profiles starts with this inversion layer and at its maximum is 1 K at the peak of the inversion (close to 2 km; Fig. 3a). Above the inversion, the potential temperature continues to increase upward with a constant dry Brunt–Väisälä frequency ($N_d = 0.01\,\mathrm{s}^{-1}$). The "dry" and "wet" tropospheric humidity profiles are similar near the surface with a near-saturated layer between 0 and 2 km (Fig. 3b). Beneath the inversion, the difference between the two profiles is 5%. In the dry profile the relative humidity drops steeply, while the wet profile features a moister troposphere. The difference above the inversion is 10% up until 10 km and then the two profiles converge by the height of 12 km. The wind speed profiles increase through the surface layer to constant values of 1, 4, and $7\,\mathrm{m\,s}^{-1}$ from the east, in keeping with an easterly trade wind direction. The characteristics of the profiles used here also broadly conform to the climatological profiles created by Dunion (2011), based on over 6000 July–October radiosondes from the Caribbean region. Note that the profile introduced by Siebesma et al. (2003) and later used by Kirshbaum and Smith (2009) is a combination of the dry atmosphere and strong inversion profiles.

The parameter choice in the prescribed atmospheric profiles leads to moist Froude numbers between approximately 0.1 and 0.7. Here the moist Froude number is defined as $F_w = UN_w^{-1}h^{-1}$, where U is the incoming flow speed, N_w is the moist Brunt–Väisälä (or buoyancy) frequency, and h is the maximum height of the mountain. Even though a Gaussian mountain is used here in order to keep the results generalized and applicable for different volcanoes, specific values were chosen to be representative for volcanic islands in the area. Depending on the particular island characteristics, F_w ranges between 0.07 and 0.63, while the aspect ratio ranges between 1.2 and 2.5 for easterly and 0.4 and 0.8 for northerly winds. Within this parameter space, it is expected that the flow will be mainly confined to a nonlinear "flow around" regime, with the higher-wind-speed cases on the border of being able to cross to the "flow over" regime (Smith 1989). However, it should be noted that in a moist atmosphere it becomes inappropriate to categorize the flow based solely on the moist Froude number, as other parameters such as CAPE and temperature inversions can heavily affect the flow (Chen and Lin 2005).

d. *Imposed temperature anomaly on the volcano summit*

The application of a suitable surface temperature anomaly at the volcano summit is now considered. Determining the surface temperature T_{sfc} of a lava dome is difficult for obvious reasons. It is clear that some kind of remote sensing is necessary to estimate a temperature. A photograph of the Soufrière Hills lava dome, presented by Macfarlane et al. (2013), is shown in Fig. 4a,

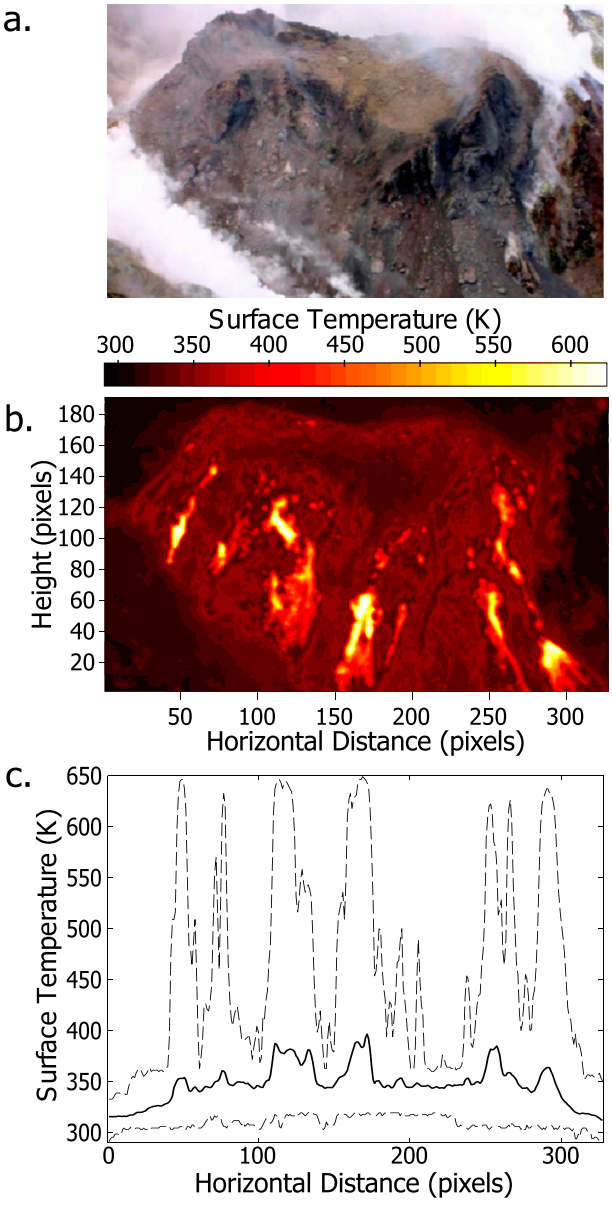

FIG. 4. The volcanic dome at Soufrière Hills Volcano, Montserrat, on 4 Nov 2005 [from Macfarlane et al. (2013)]. (a) Visible image. (b) Infrared image converted to surface temperature. Note that one pixel is approximately 1 m in both horizontal and vertical directions. (c) Mean surface temperature from (b), averaged over the vertical (solid line). The minimum and maximum temperatures at each horizontal position are shown by the dashed lines.

along with a near simultaneous surface temperature image, recorded using an infrared camera (Fig. 4b). The surface temperature ranges from 300 to 600 K, with the "hot spots" tending to be relatively small in area and associated with fissures, cracks, and fresh lava (Macfarlane et al. 2013). Away from the dome, the surface temperature quickly drops to a background temperature of approximately 300 K (periphery of Fig. 4b).

Figure 4c shows average values across the IR image, surrounded by the maximum and minimum over that height. The surface temperature distribution can be split into two parts: an average increase in temperature over the area of the dome ($T_{sfc} \simeq 350$ K) and perturbations superimposed on this average increase (T_{sfc} up to 600 K, corresponding to the yellow colors in Fig. 4b). Despite the very high surface temperatures of the hot spots, when averaged over the dome, they are typically only approximately 7-K perturbations over the relatively uniform dome anomaly.

In the WRF Model, the surface temperature in the model is specified at initialization by gradually increasing the surface temperature toward the summit. A grid spacing of 300 m was chosen, which, although sufficient for resolving orographic flows (Bryan et al. 2003), does mean the volcanic dome is only crudely resolved as a small number of grid points; that is, the fine surface temperature details of the dome (e.g., the hot spots) are not represented in the WRF surface boundary conditions. Instead surface temperature anomalies of between 0 and 60 K are specified. For a cross section across the center of the volcano (Fig. 2c) the temperature anomaly T' is imposed as a Gaussian distribution over roughly nine grid points following Eq. (2):

$$T'(x,y) = T_a \exp\left[-\left(\frac{x-x_0}{W}\right)^2 - \left(\frac{y-y_0}{W}\right)^2\right], \quad (2)$$

where T_a is the maximum temperature anomaly for each case, x_0 is the center of the dome, and W (900 m) is the characteristic horizontal length scale of the distribution. A typical dome at SHV ranges between 500 and 1000 m in diameter (Wadge et al. 2014), shaded in Fig. 2c. The surface temperature anomaly is time independent in each experiment, leading to a nearly constant surface heat flux once the simulation has reached a quasi-steady state.

As noted previously, thermal forcing due to solar heating is not studied here. Using a formula for the sensible heat flux on a lava dome (Hicks et al. 2009) and the IR data from the dome (Fig. 4), for $|U| = 1$–$7\ \mathrm{m\,s^{-1}}$ the resulting sensible heat flux can be estimated as between 100 and 750 $\mathrm{W\,m^{-2}}$, averaged over the dome. This is the same order of magnitude and up to 4 times higher than values used by relevant studies of thermal convection [e.g., 100–200 $\mathrm{W\,m^{-2}}$ in Kirshbaum (2011) and Nugent et al. (2014)] and thus, locally, is expected to have a large impact on the flow.

As the response of the flow to heated terrain has been found to be highly nonlinear (Kirshbaum 2013), the main simulations were carried out for a range from $T_a = 0$ (control runs) to $T_a = 60$ K in increments of 20 K

TABLE 1. Summary of simulations. $\overline{\text{RH}}$ is the average relative humidity across the atmosphere, θ_I is the potential temperature at the peak of the inversion, $|U|$ is the value of the easterly winds above the inversion, and T_a is the value of the temperature anomaly (0:20:60 indicates range start:increment:range end). Experiment names refer to the combination of the relative humidity and temperature inversion values.

Experiment name	$\overline{\text{RH}}$ (%)	θ_I (K)	$\lvert U\rvert$ (m s^{-1})	T_a (K)
Dry–strong inversion	50	308.2	1, 4, 7	0:20:60
Dry–weak inversion	50	307.2	1, 4, 7	0, 60
Wet–strong inversion	60	308.2	1, 4, 7	0, 60
Wet–weak inversion	60	307.2	1, 4, 7	0:20:60

(temperature forcing runs). The parameter combinations [relative humidity ($\overline{\text{RH}}$), inversion strength θ_I, wind speed $|U|$, and surface temperature forcing T_a] used in the suite of model integration are summarized in Table 1.

3. Control experiments: Flow over a mountain

Control simulations are presented in order to outline the basic flow response to the orography in the absence of any surface temperature forcing. Results are presented for three wind values ($|U|$ = 1, 4, and 7 m s^{-1}, equivalent to $F_w = 0.1, 0.4$, and 0.7), for the two "extreme" atmospheres: a dry profile with a strong inversion and a wet profile with a weak inversion—that is, those least and most conducive to moist convection. All control figures presented have the same layout: columns have the same atmospheric structure characteristics (dry–strong inversion—$\theta_I = 308.2$ K, $\overline{\text{RH}} = 50\%$ and wet–weak inversion—$\theta_I = 307.2$ K, $\overline{\text{RH}} = 60\%$), while rows have the same incoming flow speed ($|U| = 1, 4$, or 7 m s^{-1}). Note that all plots show restricted parts of the full domain and all data shown are 3-h averages.

Figure 5 shows vertical velocity on the third model level on terrain-following coordinates, overlaid with vectors for the horizontal wind. This level was chosen as it is representative of low-level flow (150 m above the surface) but outside of direct surface-layer influence. All panels show easterly flow (coming from the right) with isolated small-scale convective cells all over the domain. A number of streamlines are plotted to facilitate comparison between the different cases.

As $|U|$ increases, the simulations change from a regime of flow around the mountain, where vertical motion is constrained to isolated cells (w approximately between −0.3 and +0.3 m s^{-1}; Figs. 5a,b) to a regime of flow over the mountain with regions of ascent on the windward slopes and descent on the leeward slopes (w approximately between −1 to −2 and +1 to +2 m s^{-1} Figs. 5e,f). For very low wind speeds, the flow is heavily affected by localized circulations with numerous small-scale vortices resolved (highlighted in Fig. 5b by the collapsed streamline). At $|U| = 4$ m s^{-1}, two strong counterrotating vortices can be seen in the lee, as expected for a Froude number of 0.4 (Smolarkiewicz and Rotunno 1989). For higher wind speeds, a strong mountain wave response is triggered as the flow progresses toward the linear theory area (Smith 1989). No major changes can be seen in the general flow between the two different atmospheric structures (dry–strong and wet–weak inversion).

In contrast, the rainfall response is very different depending on the atmospheric conditions (Fig. 6). For low incoming flow speeds ($|U| = 1$ m s^{-1}), the rainfall is mainly convective. In the dry–strong inversion case, there is rainfall in the lee of the mountain as a result of leeside convergence (Roe 2005) as well as scattered rainfall as a result of individual convective cells (Fig. 6a). In the wet–weak inversion case, rainfall due to larger convective cells is visible, scattered around the domain, possibly as a result of the influence of strong individual cells in the flow (Fig. 6b). Both cases feature rainfall rates of $R > 2$ mm h^{-1}, consistent with moderate to deep convection. Note that the term "deep convection" will be used to describe rainfall associated with cloud tops above 3 km on average ($R > 2$ mm h^{-1}). This is a slightly unusual definition as it encompasses both "moderate" and deep convection (cloud tops over 5 km), but it is used to make the distinction between convection below the inversion and above.

For $|U| = 4$ m s^{-1}, there is a switch toward a more orographically forced rainfall regime, as the wind is now strong enough to disrupt the evolution of strong single convective cells (Schlesinger 1973). However, as seen in Figs. 5c and 5d, the flow is not energetic enough to go entirely over the mountain and, as such, the orographic response is minimal and can only be seen only in the wet–weak inversion case (Figs. 6c,d).

At $|U| = 7$ m s^{-1}, orographic rainfall dominates. Although convective rainfall can still be seen, elongated in the direction of the wind, the domain is now dominated by rainfall over the mountain—concentrated at the crest in the dry–strong inversion case and more widespread in the wet–weak inversion case (Figs. 6e,f). In the dry–strong inversion case, the orographic rainfall is consistent with shallow convection ($R < 2$ mm h^{-1}), while in the wet–weak inversion case deep convection ($R > 2$ mm h^{-1}) is triggered as the incoming flow is already close to saturation. Peak rainfall rates can reach approximately 20–25 mm h^{-1}, consistent with simulations of deep convection (Kirshbaum and Durran 2004) and tropical cyclone conditions (Houze et al. 2006).

Figure 7 shows a vertical cross section across the middle of the terrain in the x direction. Results are

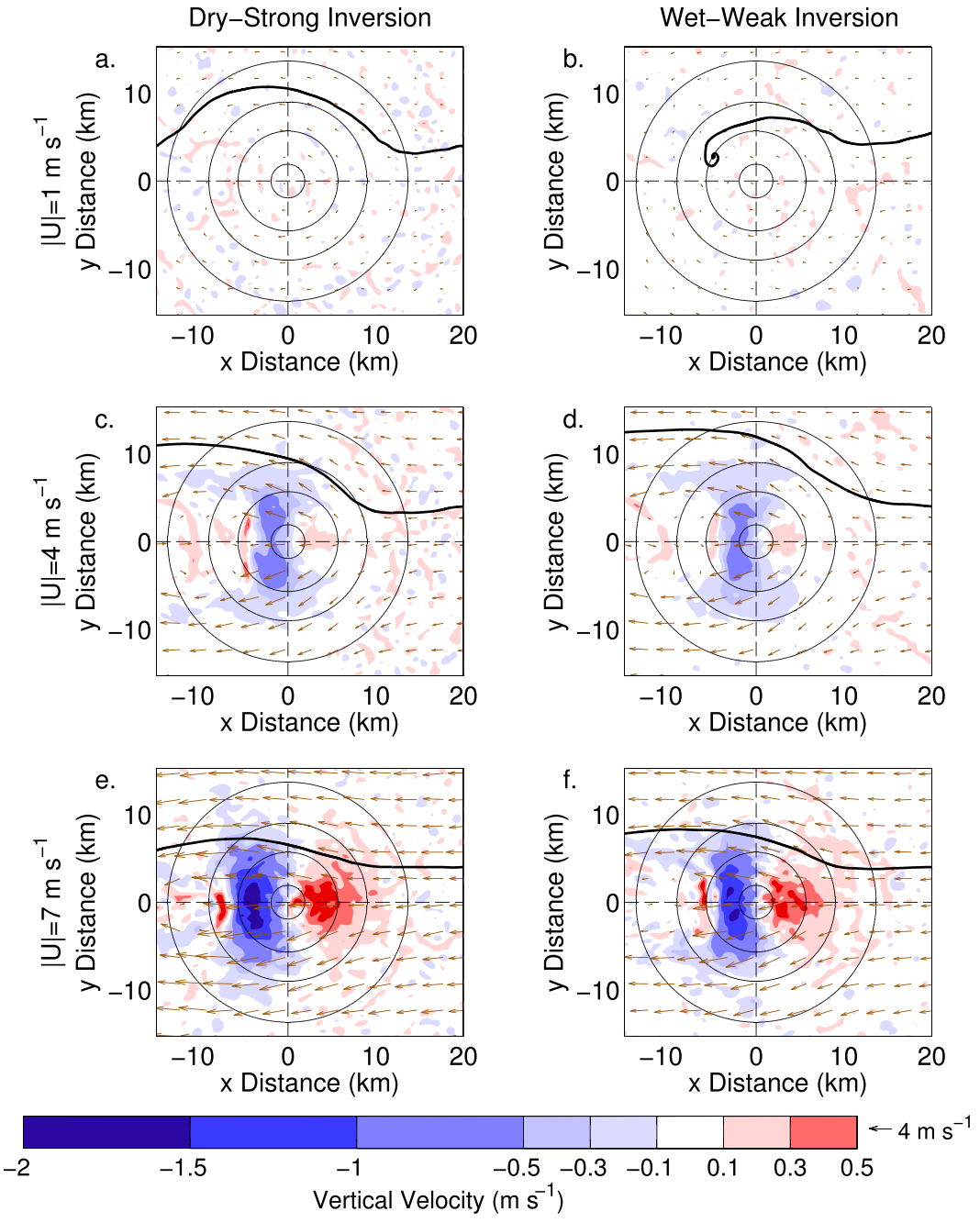

FIG. 5. Control simulations ($T_a = 0$ K). Vertical velocity (shading) with the horizontal wind vectors (every tenth vector is plotted) on the third model level. (a),(c),(e) Dry–strong and (b),(d),(f) wet–weak inversion initialization for $|U|$ = (top) 1, (middle) 4, and (bottom) 7 m s^{-1}. Note that the color bar (as in most of the figures that follow) is nonlinear near zero to make a clear distinction between positive and negative values. Streamlines shown starting at $x = 20$ km and $y = 4$ km for all cases. Height contours are at 5, 100, 500, and 900 m. The fields shown are 3-h averages.

averaged over five grid points (1.5 km) in the y direction. Each panel is split into three parts. The top part shows vertical velocity (shaded), cloud mixing ratio, and potential temperature (lines). The middle part shows mean and maximum rainfall intensity. Maximum values are values sustained for at least 30 min to filter out very high but not long-lasting rainfall rates. Finally, the bottom part shows the frequency for rainfall over three limits: 1, 5, and 10 mm h^{-1}. A frequency of 1 denotes continuous rainfall over the 3 h of integration. Note that some extreme values in both vertical velocity and rainfall can be expected if the cross section intersects a deep convective cell.

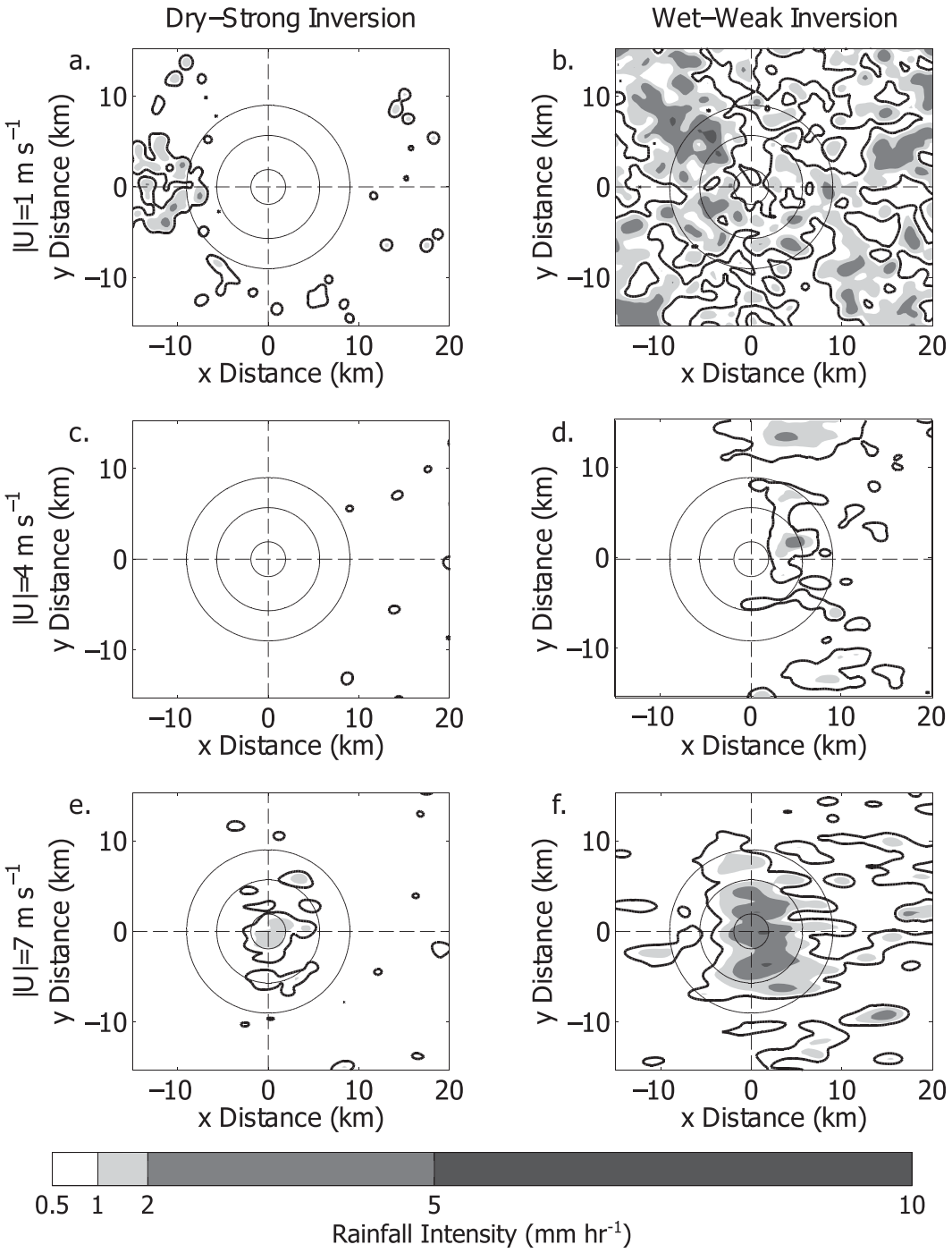

FIG. 6. As in Fig. 5, but for rainfall rate. The thick black contour signifies $R > 0.5\,\mathrm{mm\,h^{-1}}$, while shaded areas show $R > 1$, 2, and $5\,\mathrm{mm\,h^{-1}}$ from light to dark.

Figure 7 also shows the progression from the flow-around regime (flat isentropes, convective rainfall cells, no gravity waves or orographic rainfall), toward the flow-over regime. For $|U| = 1\,\mathrm{m\,s^{-1}}$ the cloud water mixing ratio is distributed fairly equally over the domain. In the dry–strong inversion case, convection is contained beneath the trade wind inversion and significant amounts of rainfall are only found in the lee of the mountain (Fig. 7a). In the wet–weak inversion case, high maximum rainfall rates ($R > 5\,\mathrm{mm\,h^{-1}}$) can be seen across the whole domain; however, these are short lived as they are not picked up by the rainfall frequency

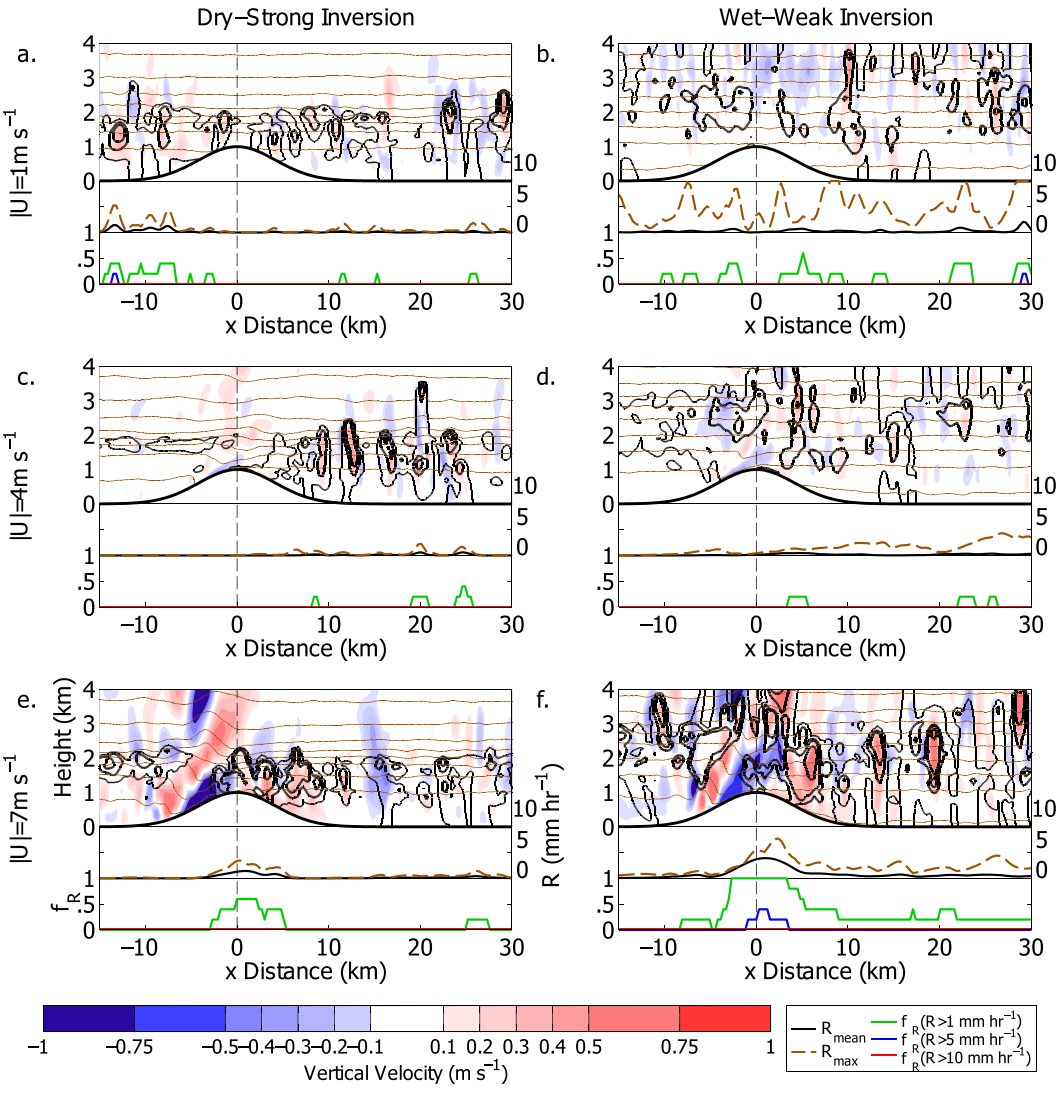

FIG. 7. Control simulations as in Fig. 5. In each panel, (top) vertical velocity (shading) with isentropes (brown lines) and cloud water mixing ratio (black lines) overlaid, along a cross section through the middle of the domain. Rainfall water mixing ratio of 0.01 g kg^{-1} is denoted by the thin black line and the cloud water mixing ratio is shown at 0.1, 0.2, 0.5, 1, and 2 g kg^{-1}. Isentropes are plotted between 299 and 307 K, every 2 K. Also shown are (middle) mean and maximum rainfall intensity (mm h^{-1}; black and brown lines; right-hand axis) and (bottom) the frequency of rainfall intensity over specific limits (green for 1 mm h^{-1}, blue for 5 mm h^{-1}, and red for 10 mm h^{-1}; left-hand axis).

distribution, pointing toward randomly distributed quick deep convective bursts that quickly get mixed with the dry air above the inversion (Fig. 7b).

For $|U| = 4\,\mathrm{m\,s^{-1}}$, the flow is more strongly controlled and the influence of the mountain is more prominent as there is a relative decrease in cloud covering in the lee. Very little rainfall is seen in either cases as the flow prohibits convective motion more strongly (Figs. 7c,d).

Finally, for $|U| = 7\,\mathrm{m\,s^{-1}}$, strong leeside descent is apparent and cloud cover greatly intensifies as the flow is forced over the mountain and is accompanied by persistent rainfall. There are mountain waves on the lee side, which are stronger in the dry–strong inversion case as the atmosphere is more strongly stratified (Figs. 7e–g). In the wet–weak inversion case, persistent deep convective rainfall can be seen (frequently over 5 mm h^{-1} over the mountain top), triggered as the more moist flow impinges on the mountain (Fig. 7f).

The control results can generally be explained in terms of the atmospheric conditions and correspond well to previous studies of similar situations (e.g., Kirshbaum and Smith 2009; Minder et al. 2013). For low incoming flow speeds, the situation can be characterized as random convection across the domain. As

the flow passes over the sea, a layer of low-level (shallow) cumulus clouds is formed beneath the inversion owing to a combination of instability beneath the inversion, convection in the boundary layer, high humidity in the atmosphere, and moisture fluxes. In the dry–strong inversion case, the convection is largely confined beneath the inversion, aside from the leeside, where there is rainfall as a result of convergence (Roe 2005). In the wet–weak inversion case, deep convective bursts appear at random over the domain, owing to the more favorable conditions for moist convection. This leads to some significant rainfall over the sea from sporadic deep convection, as the inversion is weakened and the atmosphere above the inversion becomes more humid. For low wind speeds and the dry–strong inversion experiments, although convective cells were triggered randomly in the domain, they were not strong enough to generate rainfall, in agreement with Smith et al. (2012). In the wet–weak inversion case, strong convection and deep convective rainfall is generated as a result of the decreased strength of the inversion as well as a more humid lower atmosphere. Note that a buildup in low-level humidity has been known to play a major role in initiating moist convection (Kirshbaum 2011).

As the incoming flow speed increases, random convection is inhibited and the flow enters a more mechanically driven "forced convection" regime (Smith et al. 2012). As the flow crosses over land, the cumulus field intensifies and high amounts of rainfall are consistently generated over the mountain, with an average rainfall intensity of at least $1\,\mathrm{mm\,h^{-1}}$—at least 5–10 times more that the average rainfall over the sea. In the wet–weak inversion case this increases to up to 50 times higher rainfall rates over the windward side compared to the sea, as the more moist flow meets the mountain and deep convection is consistently generated. These results are in good agreement with studies focusing on trade winds impacting on a tropical mountain (Cuijpers and Duynkerke 1993; Kirshbaum and Smith 2009; Minder et al. 2013; Cécé et al. 2014).

4. Surface heating experiments: Flow over a volcano

The response of the atmospheric circulation to the surface temperature anomaly on the volcano summit is now examined. Initially the focus is on the changes brought by differences in the surface thermal forcing for the dry–strong inversion and wet–weak inversion simulations for $|U| = 1\,\mathrm{m\,s^{-1}}$ and $T_a = 60\,\mathrm{K}$. Results from a range of T_a values are presented later in section 5.

Figure 8 shows horizontal and vertical plots of vertical velocity, horizontal wind, cloud water mixing ratio, and rainfall. Note that horizontal plots are focused on a $5 \times 5\,\mathrm{km^2}$ area at the top of the mountain, so that the resulting structure can be seen in more detail. The temperature anomaly forces a concentrated area of ascent mainly focused over the top of the mountain (Figs. 8c,d). This thermally forced ascent ($w > 1\,\mathrm{m\,s^{-1}}$) is circular and appears over and in the lee of the dome. It is surrounded by weaker, scattered convection at random ($w < 0.3\,\mathrm{m\,s^{-1}}$) in the domain.

For $T_a = 60\,\mathrm{K}$, two counterrotating vortices can be seen in the lee of the mountain top, drawing air back toward the convective plume—extra streamlines initialized at $x = 2\,\mathrm{km}$ and $y = 1\,\mathrm{km}$ emphasize this pattern. Such vortices are common features of wild fires (Cunningham et al. 2005), but in this case they do not develop the same vertical structure and are only found near the surface, possibly resulting from the strength of the forcing. Although these vortices are a ubiquitous feature in plumes, there is still debate on their generation and evolution (Cunningham et al. 2005). The plume's major impact is limited to a $2 \times 2\,\mathrm{km^2}$ area surrounding the temperature anomaly, focused toward the lee of the dome. As with the control runs (Fig. 5), the basic flow response is similar in the dry–strong inversion (Fig. 8c) and the wet–weak inversion cases (Fig. 8e).

Vertical cross sections across the middle of the domain for no surface heating show the shallow cumulus confined below the temperature inversion (Fig. 8b). However, when the surface temperature forcing is switched on, a plume accompanied by increased cloud cover is introduced. For the dry–strong inversion case, this is restricted by the temperature inversion (Fig. 8d). Some rainfall can be seen in the lee of the dome, but this is a very weak and erratic response, associated with a frequency of 0.2 for $R > 1\,\mathrm{mm\,h^{-1}}$. For the wet–weak inversion case, there is a stronger vertical development in the plume as it reaches a height of about 4 km. Rainfall is triggered beneath the plume and it is a more robust response—a frequency of 1 for $R > 1$ and $R > 5\,\mathrm{mm\,h^{-1}}$ (Fig. 8f). Stronger rainfall rates ($R > 10\,\mathrm{mm\,h^{-1}}$) also appear, at a frequency of about 0.3.

As seen here, the generation of deep convection over the lava dome is not constant but tends to happen in "bursts." Kirshbaum (2011) studied several hypotheses for initialization mechanisms of deep convection in a similar setting and argued that, instead of deep ascent of a single updraft, it is more likely that the convection is caused by a rapid succession of thermals vented through the convergence zone into a deepening cloud mass. In the context of the simulations here, we think that this is

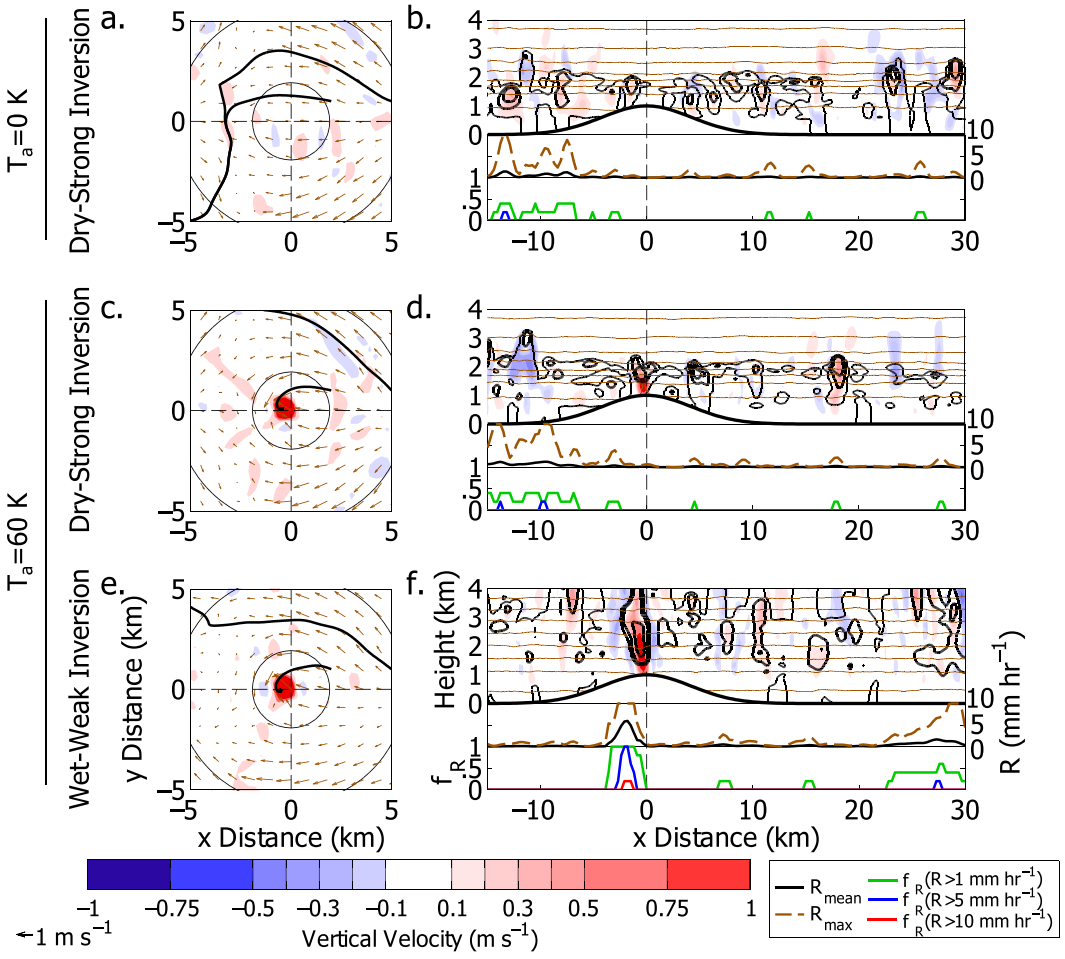

FIG. 8. Surface heating simulations. (a),(c),(e) Vertical velocity (shading) with the horizontal wind vectors (every tenth vector is plotted) on the third model level for (a) $T_a = 0$ K, dry–strong inversion; (c) $T_a = 60$ K, dry–strong inversion; and (e) $T_a = 60$ K, wet–weak inversion. Height contours at 600 and 900 m and streamlines starting at $x = 2$ and 5 km and $y = 1$ km. (b),(d),(f) (top) Vertical velocity (shading) with isentropes (brown lines) and cloud water mixing ratio (black lines) overlaid, along a cross section in the middle of the domain for the same simulations; rainwater and cloud water mixing ratio (black), isentropes (brown), and (middle),(bottom) rainfall intensity data as in Fig. 7. All results are for $|U| = 1\,\mathrm{m\,s^{-1}}$.

represented by these deep convective bursts that occur once the background state is sufficiently conditioned.

5. Volcanically triggered rainfall characteristics

In this section, the effect of the background atmospheric state (wind speed, humidity, and inversion strength) on the characteristics of the rainfall over the volcano will be examined using data from across all the atmospheric profiles and incoming flow speeds for $T_a = 60$ K (Fig. 9). As expected by the limited area of the effect, away from the lava dome, the general rainfall patterns remain largely unaffected by the surface heating. Simulations using the dry atmosphere profile (rows 1 and 2) have very similar results both when comparing the strong and weak inversion profiles and when comparing to the control simulations (Figs. 6a,c,e). As seen in section 4, the stability of the atmosphere is too strong for the surface heating to force a consistent and strong response. For simulations using the wet atmosphere profile, this changes as a patch of volcanically triggered rainfall is generated over and in the lee of the dome for $|U| < 7\,\mathrm{m\,s^{-1}}$. Specifically, for $|U| = 1\,\mathrm{m\,s^{-1}}$ this can be seen starting over the dome and extending toward the lee side for 2 km, while in the $|U| = 4\,\mathrm{m\,s^{-1}}$ the rainfall is advected farther downwind (at approximately $x = -5$ km). For stronger winds, no volcanically triggered rainfall can be seen, possibly because it is inhibited as a result of the stronger advection, mechanical mixing of the plume, and the strong downslope wind in the lee.

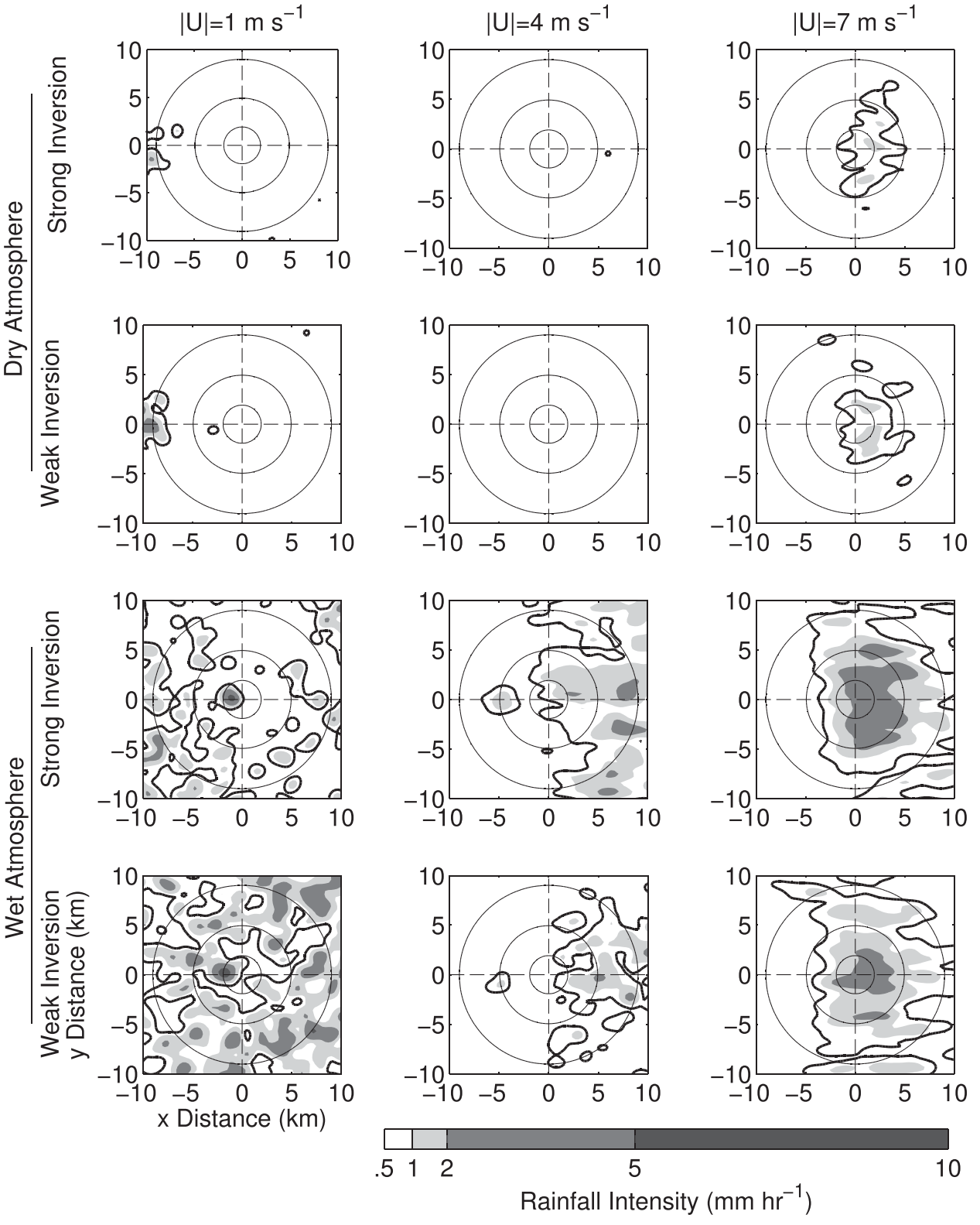

FIG. 9. Rainfall intensity over the volcano in the $T_a = 60$ K experiments for $|U|$ = (left) 1, (middle) 4, and (right) 7 m s^{-1} in (top two rows) a dry ($\overline{\mathrm{RH}} = 50\%$) and (bottom two rows) wet ($\overline{\mathrm{RH}} = 60\%$) atmosphere with a strong ($\theta_I = 308.2$ K) and a weak ($\theta_I = 307.2$ K) inversion. The thick black contour line signifies $R > 0.5$ mm h^{-1}, while shaded areas show $R > 1, 2$, and 5 mm h^{-1} from light to dark. Height contours are at 500, 700, and 900 m.

a. Incoming flow speed: Alters flow and rainfall regime

As $|U|$ increases (from left to right in Fig. 9), there is a significant change in the rainfall regime: for $|U| = 1\,\mathrm{m\,s^{-1}}$, rainfall is mainly convective and appears randomly in the domain; $|U| = 4\,\mathrm{m\,s^{-1}}$ is an intermediate case in which strong convective motion is inhibited and weak to moderate orographic rainfall can be found on the windward side depending on the atmospheric conditions; and $|U| = 7\,\mathrm{m\,s^{-1}}$ has a strong orographic response, with intense rainfall triggered persistently on the windward side and over the summit, especially for the more convective atmospheric profiles. This is consistent with the control simulations (see Fig. 6). Volcanically triggered rainfall can be seen for $|U| = 1$–$4\,\mathrm{m\,s^{-1}}$ for the wet atmosphere soundings, while any response for $|U| = 7\,\mathrm{m\,s^{-1}}$ is mixed with the increased orographic rainfall over the summit or advected downstream. For $|U|$ between 1 and $4\,\mathrm{m\,s^{-1}}$, an increase in the incoming flow speed has two effects: (i) a decrease in the average rainfall intensity and (ii) an increase in the downstream distance of the triggered rainfall from the temperature anomaly on the volcano summit.

b. Humidity: Increases total rainfall and storm size

An increase in the prescribed tropospheric relative humidity (wet atmosphere compared to dry atmosphere in Fig. 9) has a dramatic effect on the rainfall rates in general and on the generation of volcanically triggered rainfall too. It leads to significantly larger areas of all types of rainfall across the volcano—relatively high humidity is essential for the triggering of rainfall by the lava dome and also drastically changes the general atmospheric response to the mountain.

c. Inversion strength: Minor spreading of rainfall

For the dry profile simulations, the effect of the inversion strength is negligible. For the wet profile simulations, a decrease in the inversion strength has a mixed effect: for $|U| = 1\,\mathrm{m\,s^{-1}}$, a weaker inversion leads to more widely spread rainfall, but for stronger incoming wind, it seems to limit the rainfall. This could possibly be the result of mixing with drier air above the inversion. However, overall the changes are not robust and can also be attributed to the stochastic nature of rainfall generation in the model. This implies that realistic changes in the inversion strength [$O(1)$ K] are too small to qualitatively affect the rainfall distribution.

d. Vertical distribution of cloud microphysical quantities

Figure 10 shows vertical profiles of cloud water mixing ratio q_C and other hydrometeors q_H (rain, snow, ice, and graupel) for three areas: over the sea, over the windward side, and over the leeside of the mountain (marked as "sea," "windward," and "lee" on the insert in Fig. 10a). Although results are averaged over a wide area (approximately $1 \times 5\,\mathrm{km^2}$), they can be influenced if a convective cell was within the area of study. All results shown are 3-h averages for $|U| = 1\,\mathrm{m\,s^{-1}}$.

As expected, there is a notable difference between the dry–strong inversion and wet–weak inversion cases (note the change in the x axis). For the control case ($T_a = 0$ K; Fig. 10a), results are similar irrespective of the position. This agrees with the results presented previously—for low incoming flow speeds the mountain plays a lesser role. All characteristics peak beneath the inversion at a height of approximately 2 km. In the wet–weak inversion case, wider distribution can be seen for most characteristics as convection is more prevalent and the atmosphere is mixed more thoroughly. In this case, q_C is more strongly confined below the inversion, while q_H is equally distributed up to 5–6 km. There is greater variability in the distributions here, but both cloud water and hydrometeor mixing ratios are below $0.1\,\mathrm{g\,kg^{-1}}$.

For $T_a = 60$ K, there is a robust increase of both the cloud water mixing ratio and the other hydrometeors in the lee, approximately 1.2–1.5 times for the dry–strong inversion and 2–3 times for the wet–weak inversion (Figs. 10c,d). The convection structure is illustrated by an almost equal spread all the way up to the tropopause in Fig. 10d.

The hydrometeor profile for the wet–weak inversion cases shows a large decrease above a height of 4 km in the troposphere (the freezing point), where rainwater mixing ratio drops to zero and ice hydrometeors start increasing (not shown individually here). This profile matches the theoretically expected profile for an oceanic area in the tropics. For example, Zipser and Lutz (1994) showed that there is a steep decrease in the radar reflectivity above the freezing point, owing to the relative weakness of the convective cells and the inability to consistently lift raindrops above the freezing level. Furthermore, by examining lower reflectivity values, they showed that the decrease in reflectivity over the freezing point does not indicate the cloud top but rather a layer of low-reflectivity cloud—consistent with the cloud water mixing ratio profile seen here.

e. Integrated storm characteristics

As seen in Fig. 9 for both wet atmosphere cases and $|U| = 1\,\mathrm{m\,s^{-1}}$, deep convection was triggered spontaneously across the domain. However, there was a persistent increase of rainfall in the lee of the lava dome. Characteristics of this volcanically triggered rainfall will now be examined. The aim here is to identify areas of

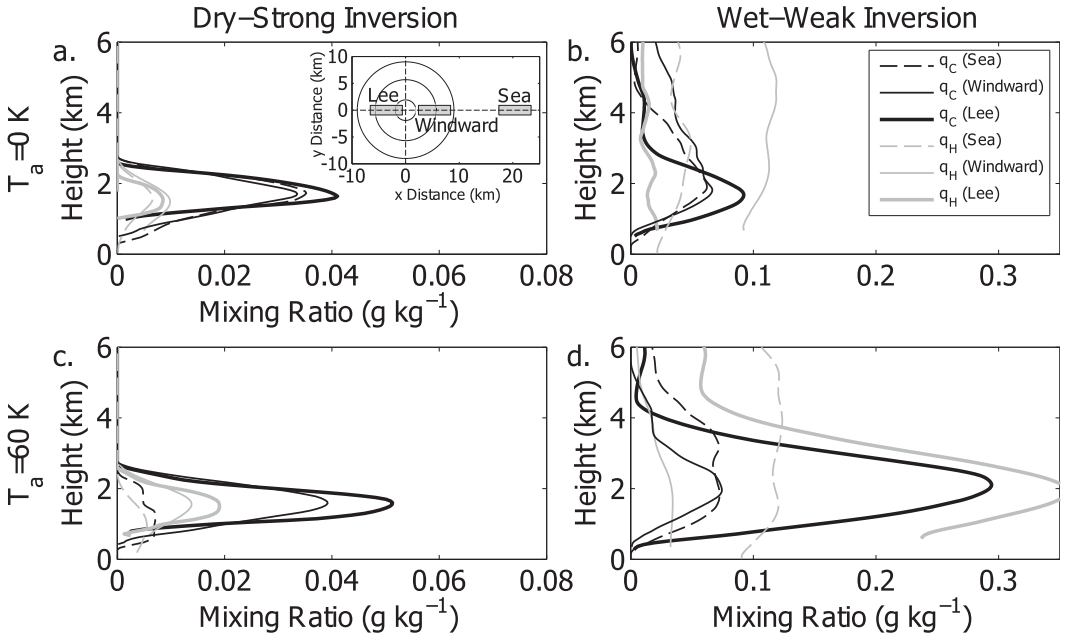

FIG. 10. Vertical profiles of cloud water mixing ratio (black) and other hydrometeors (rain, snow, ice, and graupel; gray) for locations sea, windward, and lee for $T_a = 0$ K: (a) dry–strong and (b) wet–weak inversions and $T_a = 60$ K, (c) dry–strong and (d) wet–weak inversions. Locations are shown in the insert in (a). Note the change in scale in the x axis. All results are for $|U| = 1\,\mathrm{m\,s^{-1}}$.

intense and persistent rainfall that did not occur during the control simulations. To do this, results from the control case were subtracted from the $T_a > 0$ K cases and, in order to differentiate between random, short-lived rainfall and rainfall as a response to the surface temperature anomaly, the following algorithm was devised. For each experiment and for every point in the domain, rainfall anomalies with $|R_a| > 0.1\,\mathrm{mm\,h^{-1}}$ were noted, and a population of rainfall anomaly durations D was created. The average duration $\overline{D}$ and standard deviation of the duration σ_D was then calculated for each case; for example, in the case of the wet–weak inversion profile with $T_a = 60$ K, $\overline{D} = 57$ min, and $\sigma_D = 17$ min. The average duration for the dry atmosphere profile cases was roughly 40–45 min, while for the wet atmosphere cases it was 55–60 min. For the rainfall anomaly to qualify as being persistent (so linked to the surface forcing), it had to satisfy the following conditions: (i) $D_a > \overline{D} + 2\sigma_D$ (where D_a is the duration of the potential lava-dome-generated rainfall anomaly) and (ii) it had to be located over or in the lee of the dome ($-10 < x < 1$ km).

For the dry–strong inversion experiments, no points were found to fulfil these criteria, pointing toward the fact that the rainfall in the lee was either random convection or not intense or persistent enough. In the wet–weak inversion cases, a significant area in the lee of the domain was found to have persistent rainfall (e.g., in the case of the wet–weak inversion profile with $T_a = 60$ K, $D_a = 113 \pm 22$ min). Three characteristics of this rainfall anomaly will now be examined: rainfall anomaly area (grid points in the lee of the dome that received over 0.1, 1, and $5\,\mathrm{mm\,h^{-1}}$ for at least $\overline{D} + 2\sigma_D$ min), rainfall anomaly intensity (average and maximum characteristics over these grid points sustained over different time periods), total rainfall anomaly (the product of the previous two for $R_a > 0.1\,\mathrm{mm\,h^{-1}}$ and average rainfall anomaly intensity for 3 h), as well as the maximum w over the rainfall anomaly area.

Rainfall anomaly area is studied for three thresholds: 0.1, 1, and $5\,\mathrm{mm\,h^{-1}}$ and for $|U| = 1\,\mathrm{m\,s^{-1}}$ (Fig. 11a). The first threshold shows the full extent of the lava-dome influence when considering practically all rainfall intensities. The second threshold, consistent rainfall over $1\,\mathrm{mm\,h^{-1}}$, has been linked with the remobilizing of sediment on the slopes of a volcano, while the third threshold, over $5\,\mathrm{mm\,h^{-1}}$, has been implicated in the triggering of volcanic eruptions and pyroclastic flows (Matthews et al. 2002; Barclay et al. 2006; Matthews

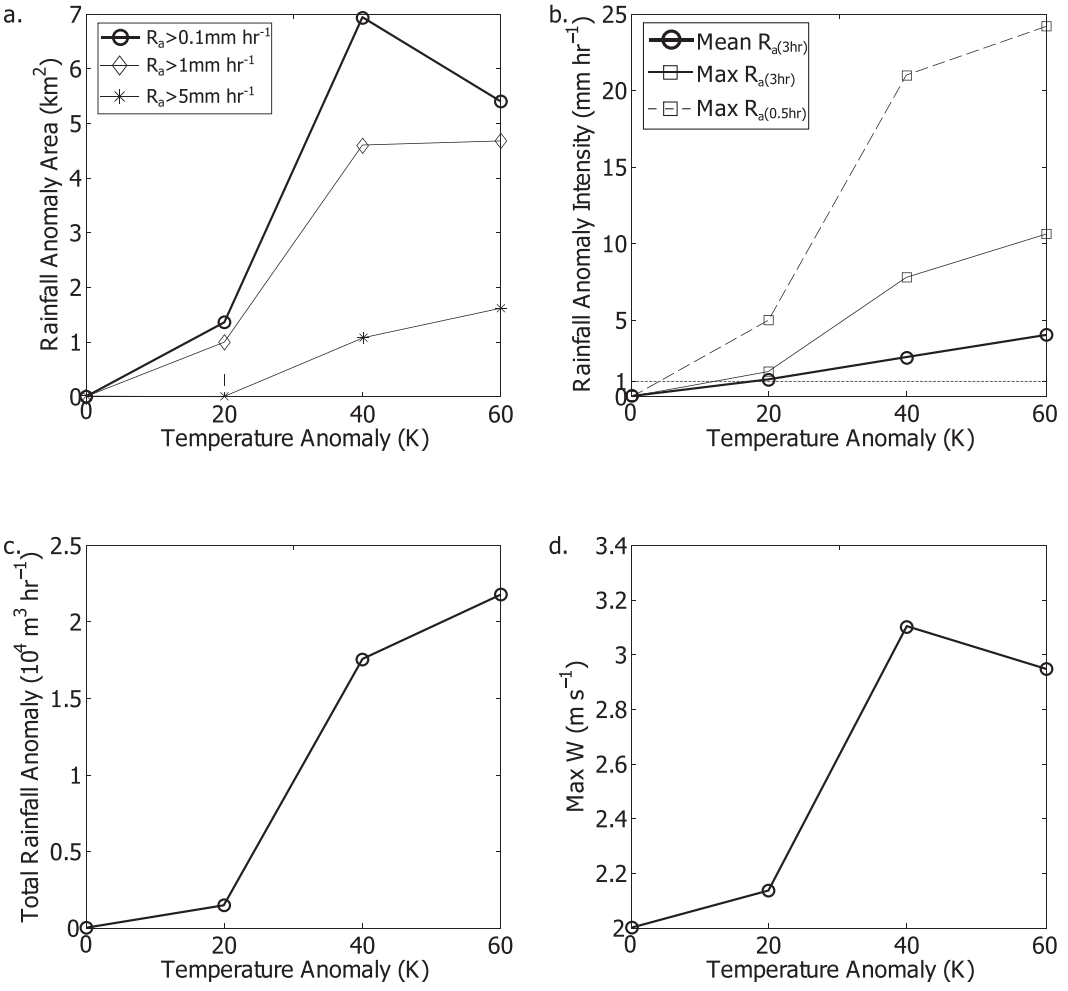

FIG. 11. Volcanically triggered rainfall characteristics for (a) rainfall anomaly area (km^2), (b) rainfall anomaly intensity ($mm\,h^{-1}$), (c) total rainfall anomaly [rainfall volume over 3 h ($m^3\,h^{-1}$)], and (d) maximum w over the rainfall anomaly area ($m\,s^{-1}$). All are plotted against temperature anomaly for wet–weak inversion simulations. We calculated (b) and (c) over the storm area. All rainfall intensities are calculated as the results from the $T_a > 0$ K cases minus the control experiments. All results are for $|U| = 1\,m\,s^{-1}$.

et al. 2009). For all rainfall intensity thresholds, rainfall anomaly area generally increases with T_a. Note that this increase is not linear—there is a significant leap in the values between $T_a = 20$ and 40 K. Results are fairly similar for $R_a > 0.1$ and $R_a > 1\,mm\,h^{-1}$, with rainfall anomaly area values at 1 km^2 for $T_a = 20$ K and 4–6 km^2 for $T_a \geq 40$ K, but rainfall anomaly area values are significantly smaller for $R_a > 5\,mm\,h^{-1}$, with 0 km^2 for $T_a = 20$ K, increasing to 1–1.5 km^2 for $T_a \geq 40$ K. Mean rainfall anomaly intensity values over the study period increase linearly with T_a, from 0 up to $5\,mm\,h^{-1}$ (Fig. 11b). This linear behavior changes when looking at the maximum rainfall intensity sustained over 3 h, with a steep gradient between $T_a = 20$ and 40 K, and becomes even more pronounced for maximum rainfall intensity sustained over 30 min. This points toward a change between $T_a = 20$ and 40 K, with deep convection triggered consistently in the latter case. Total rainfall anomaly increases by a factor of 8 between $T_a = 20$ and 40 K but then only by a factor of 1.2 between 40 and 60 K (Fig. 11c). Maximum w shows a similar behavior, with an increase from 2.1 to 3.1 $m\,s^{-1}$ between the first two experiments and then a small decrease between the last two experiments (Fig. 11d). Note that for $T_a = 0$ K the value is the maximum w up to a height of 2 km over the volcano. In short, for $T_a \geq 40$ K, consistent intense (deep convective) rainfall is triggered by the surface heating.

As seen here, once consistent deep convection is triggered (for $T_a \geq 40$ K in the experiments), the rainfall anomaly has relatively similar characteristics, with the largest changes occurring between $T_a = 20$ and 40 K.

TABLE 2. Ranking of control parameters by simulated impact for the changes of the size listed.

Control parameter	Change	Effect	Justification
T_a	$O(20)$ K	Primary	Controls the initialization and rainfall response
$\overline{\mathrm{RH}}$	$O(10)$%	Primary	Controls the initialization of rainfall
$\lvert U\rvert$	$O(3)$ m s^{-1}	Primary	Controls rainfall regimes and initiation
θ_I	$O(1)$ K	Secondary	Does not force significant changes in rainfall

This behavior points toward the fact that the temperature anomaly acts to trigger convection, but once triggered the characteristics of both the convection and the rainfall are largely controlled by realistic processes in the atmosphere. The rainfall triggered by the lava dome has also been seen to consistently be over the threshold to affect volcanic hazards around the lava dome.

Sensitivity tests carried out for a number of microphysics modules (WSM5; WSM6; Thompson, Milbrandt, and Morrison schemes; Skamarock et al. 2008) and at different grid spacings (Δx = 150 and 75 m) revealed that, aside from the well-established sensitivities in both the microphysics schemes (Otkin and Greenwald 2008) and the grid spacing (Bryan et al. 2003; Kirshbaum and Smith 2009), results were qualitatively similar, with the most changeable characteristic being the rainfall anomaly area that ranged between 5 and 9 km^2 for the different microphysics schemes and increased to 13–14 km^2 for the higher-resolution simulations.

6. Discussion

The main impact of a surface temperature anomaly on the volcano summit has been the introduction of a strong convective plume on, or just downwind, of the thermal anomaly depending on the incoming flow speed and the magnitude of the anomaly. For small values of T_a, the plume is capped by the trade wind inversion, but above a critical value of T_a (between 20 and 40 K in the simulations here), the plume breaks through the inversion and triggers a localized storm; that is, deep convection accompanied by high rainfall rates. The resulting deep convection has been shown to be sensitive to both the atmospheric conditions and the intensity of the thermal forcing although the associated rainfall intensities are less so. A drier atmosphere with a stronger inversion limits this effect as moist convection is inhibited. This leads to a plume and consistent cloud cover but not to rainfall. A moister atmosphere with a weaker inversion allows for a large area of rainfall accompanying the cloud cover. A qualitative ranking of the different control parameters by their effect on the volcanically triggered rainfall is presented in Table 2.

This rainfall has been shown to be very sensitive to the incoming flow speed. Both the area and the intensity of the rainfall can be impacted as stronger winds can severely inhibit the generation of deep convection. This high sensitivity to wind strength has been noted by Kirshbaum (2011), who found that for a mountain weakly heated by solar radiation, incoming flow speeds of over 3 m s^{-1} were enough to completely inhibit deep convection. In the experiments here an incoming flow speed of 4 m s^{-1} was found to severely limit convection but not completely inhibit it. This difference can be attributed to the intensity of the surface heating—up to 60 K, leading to almost an $O(10^3)$ W m^{-2} sensible heat flux. However, in the experiments here, this is confined to a relatively small area (approximately 1×1 km^2), leading to a strong but very localized perturbation. Further away from the thermal anomaly, the strength of the controlling parameters and the large-scale flow (stability through the inversion and to a lesser extent a weak katabatic flow) as well as the mixing with drier air above the inversion quickly dilutes the plume; that is, the storm dissipates if conditions become prohibitive. The dependence on the atmospheric conditions is clear when comparing the dry–strong inversion and wet–weak inversion simulations: a 10% increase in relative humidity and a 1-K decrease in inversion strength control the initiation of any rainfall.

The resulting rainfall intensity ranges between a few millimeters per hour sustained for several hours up to bursts of 10 mm h^{-1} sustained over shorter periods of time. Generally, rainfall over a threshold of 5 mm h^{-1} is required to initiate volcanic hazards such as lahars or explosive activity (Barclay et al. 2006). Thus, depending on the state of the dome, this initialization mechanism should be considered when dealing with hazard assessment, especially as it suggests lahars could be expected even on days when synoptic-scale rainfall is not forecast. It should be noted that for the parameter space studied here the rainfall was advected away from the immediate vicinity of the lava dome. Even though this makes a rainfall-triggered lava dome collapse feedback loop less likely, the rainfall anomaly intensity is considerably high and, because of the danger posed by the hazard, this possibility should generally be considered for days with low winds ($\lvert U\rvert < 2$ m s^{-1}). Using climatological data from Dunion (2011), an estimate can be calculated for the days volcanically triggered rainfall can be assumed

to occur. Out of the whole dataset studied, for days when the relative humidity in the lower atmosphere is over the wet atmosphere profile threshold (RH > 85%) and when wind speed is be over 2 and 4 m s^{-1}, we can estimate that some degree of volcanically triggered rainfall is expected from 4% (very low wind speeds: rainfall close to the lava dome possible, lahar triggering, and likelihood of rainfall-triggered eruption) to 18% of the time (higher wind speeds: possible lahar triggering in the lee, away from the lava dome). These calculations assume a sufficiently hot lava dome.

Both the convective plume and the resulting rainfall are in qualitative agreement with other studies in which there is thermal forcing at the surface—for example, associated with wildfires (Cunningham and Reeder 2009) or solar heating (Kirshbaum 2011). Conceptually, the mechanism is the same for all cases: a strong thermal source causes convection that may be able to overpower the convective inhibition of the atmosphere. For wildfires, a more widespread (typically kilometers in scale) thermal forcing leads to more widespread storms covering several square kilometers. For solar heating, the heating regime is usually weaker and the forcing is a function of the mountain height; thus, the area of the perturbation is the area of the mountain—typically several kilometers wide (Tian and Parker 2003; Crook and Tucker 2005; Kirshbaum 2011). In contrast, here the volcanic dome sets the scale of the storm.

In our study, the volcano is simulated simply as a realistic increase in the surface temperature (based on infrared imagery) of an otherwise passive mountain. In reality, volcanoes are a source of ash and various gaseous emissions: water vapor, carbon dioxide, sulphur dioxide, and traces of other chemicals. In SHV, Hicks et al. (2009) estimated an average total daily gas flux ranging between 0.003 and 1.5 × 10^{-3} kg s^{-1} m^{-2}, variable on many different time scales. Of this, the largest part (approximately 90%) is water vapor (Hammouya et al. 1998). Volcanic gas flux and composition, however, vary significantly between different volcanoes (Gerlach 1991). These emissions, along with the volcanic ash, are known to have an impact on cloud microphysics in the vicinity of the volcanic conduit—for example, affecting cloud seeding and other processes (Durant et al. 2008)—and has been known to cause acid rain (Lane and Gilbert 1992). However, these secondary effects were not studied here. Rather, we examined the primary response of the atmospheric flow to the increase in temperature—that is, a thermally induced convective plume. The effect of the ash and gas emissions and any interactions with the thermal circulation will need to be considered in future work, but it should be noted that the two plumes are expected to act in tandem—the gases and ash enhancing the effects of the temperature anomaly.

7. Conclusions

As moist atmospheric flow meets an obstacle, be that a mountain or a ridge, part of it is forced to ascend, which can lead to orographic precipitation. A moist flow can also interact with differentially heated terrain, as baroclinicity is created, forcing localized convection that can, under certain conditions, trigger deep convection and intense rainfall. What has been investigated here is whether a lava dome, a hot but small area on the summit of a volcano, can act to trigger deep convection on an isolated island impacted by moist easterly trade winds. A parameter space covering typical atmospheric conditions has been examined for a range of realistic volcanic surface temperature anomalies.

Depending on the prescribed conditions the volcanically heated dome can create a convective plume that penetrates through the trade wind inversion, resulting in a localized storm, with convergence into the plume from counterrotating vortices and associated high rainfall rates. For the atmospheric conditions examined, a temperature anomaly of at least 20–40 K is required to trigger a volcanic storm. Changes in the surface temperature anomaly, the relative humidity profile and incoming flow speed strongly impact the rainfall location, distribution, and amount. In particular, volcanically triggered rainfall is most distinct for low wind speeds ($|U| < 4$ m s^{-1}). Modest changes in the inversion strength have a secondary impact.

The simulations presented here are highly idealized. The effects of volcanic emissions, a source of both water vapor and cloud nuclei, as well as short- and longwave radiation, are not considered and simplifications of topography, heating, and the atmospheric conditions have been made. Nevertheless, care has been taken to keep the simulations realistic and general. As such, this kind of triggering of deep convection is possible for any active volcano, not undergoing an explosive eruption, provided that the forcing and atmospheric conditions are fulfilled. Consequently, the rainfall-generation mechanism proposed here will affect the weather and climate locally and could have an impact on volcanic hazards such as pyroclastic flows, lahars, or debris flows. Indeed, this mechanism could offer an explanation for occurrences of volcanic hazards on days with little or no synoptic-scale rainfall in various volcanoes in the tropics.

Acknowledgments. The research presented in this paper was carried out on the High Performance Computing Cluster supported by the Research and Specialist

Computing Support service at the University of East Anglia. The authors thank David MacFarlane for the lava-dome image; the WRF Help email assistance service; Daniel Kirshbaum, Ralf Toumi, and Roland von Glasow for useful discussions; and three anonymous reviewers for their helpful comments.

REFERENCES

Barclay, J., J. E. Johnstone, and A. J. Matthews, 2006: Meteorological monitoring of an active volcano: Implications for eruption prediction. *J. Volcanol. Geotherm. Res.*, **150**, 339–358, doi:10.1016/j.jvolgeores.2005.07.020.

Beljaars, A. C. M., 1995: The parameterization of surface fluxes in large-scale models under free convection. *Quart. J. Roy. Meteor. Soc.*, **121**, 255–270, doi:10.1002/qj.49712152203.

Bryan, G. H., J. C. Wyngaard, and J. M. Fritsch, 2003: Resolution requirements for the simulations of deep moist convection. *Mon. Wea. Rev.*, **131**, 2394–2416, doi:10.1175/1520-0493(2003)131<2394:RRFTSO>2.0.CO;2.

Carn, S. A., R. B. Watts, G. Thompson, and G. E. Norton, 2004: Anatomy of a lava dome collapse: The 20 March 2000 event at Soufrière Hills Volcano, Montserrat. *J. Volcanol. Geotherm. Res.*, **131**, 241–264, doi:10.1016/S0377-0273(03)00364-0.

Cécé, R., D. Bernard, C. d'Alexis, and J.-F. Dorville, 2014: Numerical simulations of island-induced circulations and windward katabatic flow over the Guadeloupe archipelago. *Mon. Wea. Rev.*, **142**, 850–867, doi:10.1175/MWR-D-13-00119.1.

Chen, S.-H., and Y.-L. Lin, 2005: Orographic effects on a conditionally unstable flow over an idealized three-dimensional mesoscale mountain. *Meteor. Atmos. Phys.*, **88**, 1–21, doi:10.1007/s00703-003-0047-6.

Crook, N. A., and D. F. Tucker, 2005: Flow over heated terrain. Part I: Linear theory and idealized numerical simulations. *Mon. Wea. Rev.*, **133**, 2552–2564, doi:10.1175/MWR2964.1.

Cuijpers, J. W. M., and P. G. Duynkerke, 1993: Large eddy simulation of trade wind cumulus clouds. *J. Atmos. Sci.*, **50**, 3894–3908, doi:10.1175/1520-0469(1993)050<3894:LESOTW>2.0.CO;2.

Cunningham, P., and M. J. Reeder, 2009: Severe convective storms initiated by intense wildfires: Numerical simulations of pyro-convection and pyro-tornadogenesis. *Geophys. Res. Lett.*, **36**, L12812, doi:10.1029/2009GL039262.

——, S. L. Goodrick, M. Y. Hussaini, and R. R. Linn, 2005: Coherent vertical structures in numerical simulations of buoyant plumes from wildland fires. *Int. J. Wildland Fire*, **14**, 61–75, doi:10.1071/WF04044.

Drazin, P. G., 1961: On the steady flow of a fluid of variable density past an obstacle. *Tellus*, **13**, 239–251, doi:10.1111/j.2153-3490.1961.tb00081.x.

Dunion, J. P., 2011: Rewriting the climatology of the tropical North Atlantic and Caribbean Sea atmosphere. *J. Climate*, **24**, 893–908, doi:10.1175/2010JCLI3496.1.

Durant, A. J., R. A. Shaw, W. I. Rose, Y. Mi, and G. G. J. Ernst, 2008: Ice nucleation and overseeding of ice in volcanic clouds. *J. Geophys. Res.*, **113**, 1984–2012, doi:10.1029/2007JD009064.

Dyer, A. J., and B. B. Hicks, 1970: Flux-gradient relationships in the constant flux layer. *Quart. J. Roy. Meteor. Soc.*, **96**, 715–721, doi:10.1002/qj.49709641012.

Eliassen, A., and E. Palm, 1961: On the transfer of energy in stationary mountain waves. *Geophys. Norv.*, **22**, 1–23.

Gatebe, C. K., T. Varnai, R. Poudyal, C. Ichoku, and M. D. King, 2012: Taking the pulse of pyrocumulus clouds. *Atmos. Environ.*, **52**, 121–130, doi:10.1016/j.atmosenv.2012.01.045.

Gerlach, T. M., 1991: Present-day co_2 emissions from volcanos. *Eos, Trans. Amer. Geophys. Union*, **72**, 249–255, doi:10.1029/90EO10192.

Hammouya, G., P. Allard, P. Jean-Baptiste, F. Parello, M. P. Semet, and S. R. Young, 1998: Pre- and syn-eruptive geochemistry of volcanic gases from Soufrière Hills of Montserrat, West Indies. *Geophys. Res. Lett.*, **25**, 3685–3688, doi:10.1029/98GL02321.

Hicks, P. D., A. J. Matthews, and M. J. Cooker, 2009: Thermal structure of a gas-permeable lava dome and timescale separation in its response to perturbation. *J. Geophys. Res.*, **114**, B07201, doi:10.1029/2008JB006198.

——, ——, and ——, 2010: Triggering of a volcanic dome collapse by rainwater infiltration. *J. Geophys. Res.*, **115**, B09212, doi:10.1029/2009JB006831.

——, M. J. Cooker, and A. J. Matthews, 2014: Saturation front evolution for liquid infiltration into a gas filled porous medium with counter-current flow. *Eur. J. Mech.*, **43B**, 202–215, doi:10.1016/j.euromechflu.2013.09.001.

Hong, S.-Y., and J.-O. J. Lin, 2006: The WRF Single-Moment 6-Class Microphysics Scheme (WSM6). *J. Korean Meteor. Soc.*, **42**, 129–151.

Hort, M., R. Seyfried, and M. Vöge, 2003: Radar Doppler velocimetry of volcanic eruptions: Theoretical considerations and quantitative documentation of changes in eruptive behaviour at Stromboli volcano, Italy. *Geophys. J. Int.*, **154**, 515–532, doi:10.1046/j.1365-246X.2003.01982.x.

Houze, R. A., Jr., 2012: Orographic effect on precipitating clouds. *Rev. Geophys.*, **50**, RG1001, doi:10.1029/2011RG000365.

——, and Coauthors, 2006: The hurricane rainband and intensity change experiment: Observations and modeling of Hurricanes Katrina, Ophelia, and Rita. *Bull. Amer. Meteor. Soc.*, **87**, 1503–1521, doi:10.1175/BAMS-87-11-1503.

Kirshbaum, D. J., 2011: Cloud-resolving simulations of deep convection over a heated mountain. *J. Atmos. Sci.*, **68**, 361–378, doi:10.1175/2010JAS3642.1.

——, 2013: On thermally forced circulations over heated terrain. *J. Atmos. Sci.*, **70**, 1690–1709, doi:10.1175/JAS-D-12-0199.1.

——, and D. R. Durran, 2004: Factors governing cellular convection in orographic precipitation. *J. Atmos. Sci.*, **61**, 682–698, doi:10.1175/1520-0469(2004)061<0682:FGCCIO>2.0.CO;2.

——, and R. B. Smith, 2009: Orographic precipitation in the tropics: Large-eddy simulations and theory. *J. Atmos. Sci.*, **66**, 2559–2578, doi:10.1175/2009JAS2990.1.

——, and J. Fairman Jr., 2014: Cloud trails past the Lesser Antilles. *Mon. Wea. Rev.*, **143,** 995–1017, doi:10.1175/MWR-D-14-00254.1.

Klemp, J. B., J. Dudhia, and A. D. Hassiotis, 2008: An upper gravity-wave absorbing layer for NWP applications. *Mon. Wea. Rev.*, **136**, 3987–4004, doi:10.1175/2008MWR2596.1.

Knievel, J. C., G. H. Bryan, and J. P. Hacker, 2007: Explicit numerical diffusion in the WRF Model. *Mon. Wea. Rev.*, **135**, 3808–3824, doi:10.1175/2007MWR2100.1.

Lane, S. J., and J. S. Gilbert, 1992: Electric potential gradient changes during explosive activity at Sakurajima volcano, Japan. *Bull. Volcanol.*, **54**, 590–594, doi:10.1007/BF00569942.

Lewis, H. W., S. D. Mobbs, S. B. Vosper, and A. R. Brown, 2008: The effect of surface heating on hill-induced flow separation. *Bound.-Layer Meteor.*, **129**, 269–287, doi:10.1007/s10546-008-9311-0.

Lin, Y.-L., R. D. Rarley, and H. D. Orville, 1983: Bulk parameterization of the snow field in a cloud model. *J. Climate Appl. Meteor.*, **22**, 1065–1092, doi:10.1175/1520-0450(1983)022<1065:BPOTSF>2.0.CO;2.

Macfarlane, D. G., H. M. Odbert, D. A. Robertson, M. R. James, H. Pinkerton, and G. Wadge, 2013: Topographic and thermal mapping of volcanic terrain using the AVTIS ground-based 94-GHz dual-mode radar/radiometric imager. *IEEE Trans. Geosci. Remote Sens.*, **51**, 455–472, doi:10.1109/TGRS.2012.2202667.

Major, J. J., and C. G. Newhall, 1989: Snow and ice perturbation during historical volcanic eruptions and the formation of lahars and floods. *Bull. Volcanol.*, **52**, 1–27, doi:10.1007/BF00641384.

Mastin, L. G., 1994: Explosive tephra emissions at Mount St. Helens, 1989–1991: The violent escape of magmatic gas following storms? *Geol. Soc. Amer. Bull.*, **106**, 175–185, doi:10.1130/0016-7606(1994)106<0175:ETEAMS>2.3.CO;2.

Matthews, A. J., and J. Barclay, 2004: A thermodynamical model for rainfall-triggered volcanic dome collapse. *Geophys. Res. Lett.*, **31**, L05614, doi:10.1029/2003GL019310.

——, ——, S. Carn, G. Thompson, J. Alexander, R. Herd, and C. Williams, 2002: Rainfall-induced volcanic activity in Montserrat. *Geophys. Res. Lett.*, **29**, doi:10.1029/2002GL014863.

——, ——, and J. E. Johnstone, 2009: The fast response of volcano-seismic activity to intense precipitation: Triggering of primary volcanic activity by rainfall at Soufrière Hills Volcano, Montserrat. *J. Volcanol. Geotherm. Res.*, **184**, 405–415, doi:10.1016/j.jvolgeores.2009.05.010.

Minder, J. R., R. B. Smith, and A. D. Nugent, 2013: The dynamics of ascent-forced orographic convection in the tropics: Results from Dominica. *J. Atmos. Sci.*, **70**, 4067–4088, doi:10.1175/JAS-D-13-016.1.

Monin, A. S., and A. Obukhov, 1954: Basic laws of turbulent mixing in the surface layer of the atmosphere. *Contrib. Geophys. Inst. Acad. Sci. USSR*, **151**, 163–187.

Nugent, A. D., R. B. Smith, and J. R. Minder, 2014: Wind speed control of tropical orographic convection. *J. Atmos. Sci.*, **71**, 2695–2712, doi:10.1175/JAS-D-13-0399.1.

Ólafsson, H., and P. Bougeault, 1996: Nonlinear flow past an elliptic mountain ridge. *J. Atmos. Sci.*, **53**, 2465–2489, doi:10.1175/1520-0469(1996)053<2465:NFPAEM>2.0.CO;2.

Otkin, J. A., and T. J. Greenwald, 2008: Comparison of WRF Model-simulated and MODIS-derived cloud data. *Mon. Wea. Rev.*, **136**, 1957–1970, doi:10.1175/2007MWR2293.1.

Paulson, C. A., 1970: The mathematical representation of wind speed and temperature profiles in the unstable atmospheric surface layer. *J. Appl. Meteor.*, **9**, 857–861, doi:10.1175/1520-0450(1970)009<0857:TMROWS>2.0.CO;2.

Queney, P., 1948: The problem of airflow over mountains: A summary of theoretical studies. *Bull. Amer. Meteor. Soc.*, **29**, 16–26.

Roe, G. H., 2005: Orographic precipitation. *Annu. Rev. Earth Planet. Sci.*, **33**, 645–671, doi:10.1146/annurev.earth.33.092203.122541.

Rutledge, S. A., and P. V. Hobbs, 1983: The mesoscale and microscale structure and organization of clouds and precipitation in mid-latitude cyclones. Part VIII: A model for the "seeder-feeder" process in warm-frontal rainbands. *J. Atmos. Sci.*, **40**, 1185–1206, doi:10.1175/1520-0469(1983)040<1185:TMAMSA>2.0.CO;2.

Schlesinger, R. E., 1973: A numerical model of deep moist convection: Part I. Comparative experiments for variable ambient moisture and wind shear. *J. Atmos. Sci.*, **30**, 835–856, doi:10.1175/1520-0469(1973)030<0835:ANMODM>2.0.CO;2.

Siebesma, A. P., and Coauthors, 2003: A large eddy simulation intercomparison study of shallow cumulus convection. *J. Atmos. Sci.*, **60**, 1201–1219, doi:10.1175/1520-0469(2003)60<1201:ALESIS>2.0.CO;2.

Simkin, S., and L. Siebert, 1994: *Catalogue of Active Volcanoes of the World*. International Association of Volcanology and Earth's Interior, 349 pp.

Skamarock, W. C., and Coauthors, 2008: A description of the Advanced Research WRF version 3. NCAR Tech. Note NCAR/TN-475+STR, 113 pp. [Available online at http://www.mmm.ucar.edu/wrf/users/docs/arw_v3_bw.pdf.]

Smith, G. A., and W. J. Fritz, 1989: Volcanic influences on terrestrial sedimentation. *Geology*, **17**, 375–376, doi:10.1130/0091-7613(1989)017<0375:VIOTS>2.3.CO;2.

Smith, R. B., 1980: Linear theory of stratified hydrostatic flow past an isolated mountain. *Tellus*, **32**, 348–364, doi:10.1111/j.2153-3490.1980.tb00962.x.

——, 1989: Hydrostatic airflow over mountains. *Advances in Geophysics*, Vol. 31, Academic Press, 1–41, doi:10.1016/S0065-2687(08)60052-7.

——, P. Schaffer, D. J. Kirshbaum, and E. Regina, 2009: Orographic precipitation in the tropics: Experiments in Dominica. *J. Atmos. Sci.*, **66**, 1698–1716, doi:10.1175/2008JAS2920.1.

——, and Coauthors, 2012: Orographic precipitation in the tropics: The Dominica experiment. *Bull. Amer. Meteor. Soc.*, **93**, 1567–1579, doi:10.1175/BAMS-D-11-00194.1.

Smolarkiewicz, P. K., and R. Rotunno, 1989: Low Froude number flow past three-dimensional obstacles. Part I: Baroclinically generated lee vortices. *J. Atmos. Sci.*, **46**, 1154–1164, doi:10.1175/1520-0469(1989)046<1154:LFNFPT>2.0.CO;2.

Sparks, R. S. J., and S. R. Young, 2002: The eruption of Soufrière Hills Volcano, Montserrat (1995-1999): Overview of scientific results. *Geol. Soc. London Mem.*, **21**, 45–69, doi:10.1144/GSL.MEM.2002.021.01.03.

Tian, W., and D. J. Parker, 2003: A modeling study and scaling analysis of orographic effects on boundary layer shallow convection. *J. Atmos. Sci.*, **60**, 1981–1991, doi:10.1175/1520-0469(2003)060<1981:AMSASA>2.0.CO;2.

Tucker, D. F., and N. A. Crook, 2005: Flow over heated terrain. Part II: Generation of convective precipitation. *Mon. Wea. Rev.*, **133**, 2565–2582, doi:10.1175/MWR2965.1.

Violette, S., G. de Marsily, J. P. Carbonnel, P. Goblet, E. Ledoux, S. M. Tijani, and G. Vouille, 2001: Can rainfall trigger volcanic eruptions? A mechanical stress model of an active volcano: 'Piton de la Fournaise', Reunion Island. *Terra Nova*, **13**, 18–24, doi:10.1046/j.1365-3121.2001.00297.x.

Voight, B., E. K. Constantine, S. Siswowidjoyo, and R. Torley, 2000: Historical eruptions of Merapi Volcano, Central Java, Indonesia, 1768–1998. *J. Volcanol. Geotherm. Res.*, **100**, 69–138, doi:10.1016/S0377-0273(00)00134-7.

Wadge, G., B. Voight, R. S. J. Sparks, P. D. Cole, S. C. Loughlin, and R. E. A. Robertson, 2014: An overview of the eruption of Soufrière Hills Volcano, Montserrat from 2000 to 2010. *Geol. Soc. London Mem.*, **39**, 1–40, doi:10.1144/M39.1.

Webb, E. K., 1970: Profile relationships: The log-linear range, and extension to strong stability. *Quart. J. Roy. Meteor. Soc.*, **96**, 67–90, doi:10.1002/qj.49709640708.

Yamasato, H., S. Kitagawa, and M. Komiya, 1998: Effect of rainfall on dacitic lava dome collapse at Unzen volcano, Japan. *Pap. Meteor. Geophys.*, **48**, 73–78, doi:10.2467/mripapers.48.73.

Zipser, E. J., and K. R. Lutz, 1994: Vertical profile of radar reflectivity of convective cells: A strong indicator of storm intensity and lightning probability? *Mon. Wea. Rev.*, **122**, 1751–1759, doi:10.1175/1520-0493(1994)122<1751:TVPORR>2.0.CO;2.